ACCSCIENCE PUBLISHING

International Journal of Bioprinting

RESEARCH ARTICLE

# 3D-printed HA/PCL composite scaffolds facilitate bone regeneration via concurrent direct osteogenesis and pro-healing macrophage polarization

**Jiaxiang Song[1,2†], Weihua Huang[2,3†], Guangquan Zhao[1,2†], Qinghong Fan[1], Qian Du[1], Yuanhao Lv[1,2], Shuai Huang[4*], Weikang Xu[2,5*], and Qingde Wa[1*]**

[1]Department of Orthopaedic Surgery, The Second Affiliated Hospital of Zunyi Medical University, Zunyi, Guizhou, China

[2]Institute of Biological and Medical Engineering, Guangdong Academy of Sciences, Guangzhou, Guangdong, China

[3]Department of Burns and Plastic Surgery, The Affiliated Qingyuan Hospital, Guangzhou Medical University, Qingyuan, Guangdong, China

[4]Department of Orthopaedic Surgery, The First People's Hospital of Foshan, Foshan, Guangdong, China

[5]Guangdong Provincial Key Laboratory of Medical Electronic Instruments and Materials, National Engineering Research Center for Healthcare Devices, Guangdong Institute of Medical Instruments, Guangzhou, Guangdong, China

[†]*These authors contributed equally to this work.*

***Corresponding authors:**
Qingde Wa
(wqd887zsy@126.com);
Weikang Xu
(759200816@qq.com);
Shuai Huang
(huangshuai85315@163.com)

**Citation:** Song J, Huang W, Zhao G, *et al*. 3D-printed HA/PCL composite scaffolds facilitate bone regeneration via concurrent direct osteogenesis and pro-healing macrophage polarization. *Int J Bioprint*.
doi: 10.36922/IJB026420456

**Received:** October 18, 2026

**Revised:** November 12, 2026

**Accepted:** November 16, 2026

**Published online:** November 25, 2026

**Copyright:** © 2026 Author(s). This is an Open-Access article distributed under the terms of the Creative Commons Attribution License, permitting distribution, and reproduction in any medium, provided the original work is properly cited.

**Publisher's Note:** AccScience Publishing remains neutral with regard to jurisdictional claims in published maps and institutional affiliations.

## Abstract

Three-dimensional (3D)-printed polycaprolactone (PCL) scaffolds are limited by bio-inertness and modest immunomodulatory capacity. Although nano-hydroxyapatite (nHA) improves osteoconductivity, how graded nHA loadings influence cytocompatibility, direct osteogenesis, and host osteoimmune responses remains unclear. Here, 3D-printed scaffolds of pure PCL, HP(2:10) (16.7 wt% nHA), and HP(3:10) (23.1 wt% nHA) were fabricated under identical printing parameters and evaluated. nHA incorporation lowered the apparent water contact angle. In contrast, compressive strength peaked in HP(2:10). Compressive modulus was higher in HP(3:10) than in HP(2:10). Among the groups tested, HP(2:10) showed the best cytocompatibility and the highest alkaline phosphatase activity (9.2 U/mg protein) and osteogenic gene expression (*Runx2*, *Col1*, *Opn*, *Bmp2*) in rat bone marrow mesenchymal stem cells. In RAW264.7 macrophages, it was associated with higher CD206 and interleukin-10 (IL-10) and lower IL-1β and IL-12, and exploratory RNA sequencing of candidate differentially expressed genes suggested enrichment of inflammatory signaling pathways, mainly the IL-17 and Toll-like receptor pathways. In a rat calvarial defect model, HP(2:10) yielded the highest bone volume fraction (20.8% at 8 weeks vs. 13.0% for PCL and 16.3% for HP[3:10]), bone mineral density, and collagen deposition, together with larger VEGF-, BMP-2-, and CD163-positive areas and a smaller iNOS-positive area. These findings suggest that an intermediate nHA loading concurrently supports direct osteogenesis and a favorable osteoimmune microenvironment among the compositions tested. Because osteogenic and macrophage responses were examined separately and only two loadings were compared, causal interplay and the effective loading range remain to be defined.

***Keywords:*** Hydroxyapatite; Polycaprolactone; 3D printing; Immunomodulation; Bone regeneration

## 1. Introduction

Large segmental bone defects resulting from severe trauma, oncological resection, or congenital malformations remain a major challenge in orthopedic surgery, frequently leading to delayed union, nonunion, and long-term functional impairment.[1] Although autologous bone grafting is still considered the clinical gold standard, its use is limited by donor-site morbidity, restricted graft availability, and secondary surgical risks.[2] These challenges have driven sustained interest in synthetic bone substitutes that combine osteoconductivity, structural support, and controlled biodegradability.[3] In this context, three-dimensional (3D) printing has emerged as an important biofabrication strategy, allowing the customized fabrication of patient-specific scaffolds with well-defined interconnected pore architectures and reproducible biomechanical properties.

Among synthetic polymers, polycaprolactone (PCL) is widely used for bone scaffolding owing to its favorable melt-extrusion printability, biocompatibility, and slow degradation rate that matches new bone remodeling.[4] However, the inherent hydrophobicity and bio-inert nature of pure PCL restrict initial cell adhesion and direct osteogenic performance.[5] To address this limitation, calcium phosphate-based bioceramics, particularly nano-hydroxyapatite (nHA), are commonly incorporated into the PCL matrix to improve surface hydrophilicity and mimic the inorganic phase of native bone.[6] Previous studies have fabricated HA/PCL composite scaffolds with HA loadings most commonly within 10–40 wt%, showing that HA inclusion enhances compressive modulus and supports osteogenic differentiation.[7-9] Nonetheless, most of these investigations focused on mechanical behavior and direct osteogenesis, often implicitly assuming improvement with increasing HA content, whereas the balance among cytocompatibility, bioactivity, and host immune response has received less attention.[10,11] Excessive bioceramic incorporation may cause particle agglomeration or local cellular stress,[12-14] dose-dependent cytocompatibility has also been reported in other nanoparticle-containing composites,[15] and balancing functional components against biocompatibility is a general consideration in bioactive composite design.[16] Systematic comparison of graded loadings is therefore warranted.

Beyond intrinsic osteoconductivity, bone regeneration *in vivo* is strongly influenced by the host immune response, a concept termed osteoimmunomodulation.[17,18] Macrophages play a central role in the bone healing microenvironment: prolonged pro-inflammatory M1-like activation promotes tissue damage and fibrous encapsulation, whereas a timely transition toward an anti-inflammatory, M2-like phenotype favors resolution of inflammation and provides a supportive niche for tissue regeneration.[19,20] Although macrophage activation is better described as a continuum than a strict M1/M2 dichotomy,[21] M1- and M2-associated markers remain widely used to characterize immune responses to biomaterials.[19,20] Emerging evidence indicates that biomaterial physicochemical cues and calcium phosphate-related ionic microenvironments can modulate macrophage polarization.[22,23] Scaffold-guided bone repair may therefore benefit from both direct osteoinductive stimulation and a favorable osteoimmune microenvironment, yet how graded HA loadings influence these two aspects remains insufficiently understood.

In the present study, 3D-printed nHA/PCL composite scaffolds with graded nHA loadings, namely pure PCL, HP(2:10), and HP(3:10) (nHA:PCL mass ratios of 2:10 and 3:10, corresponding to 16.7 and 23.1 wt% nHA, respectively), were fabricated under identical printing parameters so that composition could be compared with comparable scaffold architecture. *In vitro* experiments with rat bone marrow mesenchymal stem cells (rBMSCs) and RAW264.7 macrophages were used to assess cytocompatibility, osteogenic differentiation, and macrophage marker responses. To explore candidate transcriptomic responses underlying the macrophage phenotypes, RNA sequencing (RNA-seq) was performed on macrophages cultured with HP(2:10). Finally, a critical-sized rat calvarial defect model was used to investigate whether the effects of a moderate nHA loading observed *in vitro* were associated with improved bone regeneration and a more favorable local immune response *in vivo* (Figure 1).

## 2. Materials and methods

### 2.1. Materials and equipment

Polycaprolactone (molecular weight 54,000 Da) was obtained from Jinan Daigang Biotechnology Co., Ltd. (China), and nHA (mean particle size 20 nm) was purchased from Engineering For Life (China). rBMSCs and RAW264.7 macrophages were purchased from Feng Hui Biotechnology Co., Ltd. (China). Standard tissue culture polystyrene (TCPS) wells were used for scaffold-

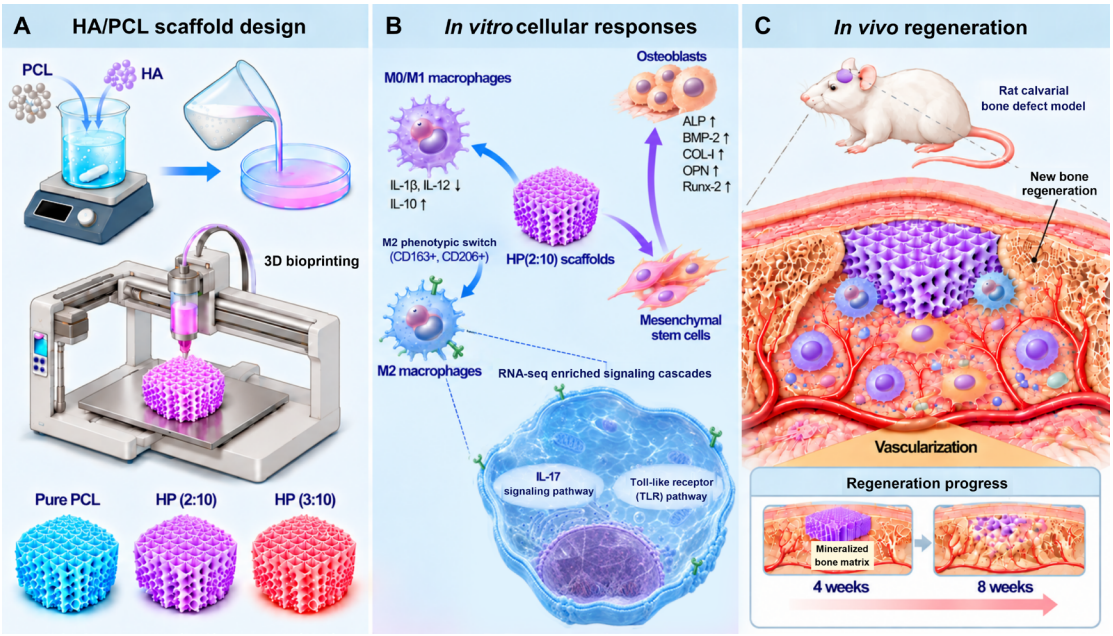



**Figure 1.** Schematic overview of nano-hydroxyapatite (nHA)/polycaprolactone (PCL) scaffold fabrication and its effects on osteogenic differentiation, macrophage responses, and bone regeneration. (A) PCL and nHA were mixed in solution, cast into films, and subsequently processed for extrusion-based 3D printing to produce pure PCL, HP(2:10), and HP(3:10) scaffolds. (B) *In vitro* evaluation showed enhanced osteogenic differentiation of rat bone marrow mesenchymal stem cells (rBMSCs) under osteogenic induction conditions and an M2-like marker profile in RAW264.7 macrophages exposed to HP(2:10). Exploratory RNA-sequencing analysis of candidate differentially expressed genes suggested enrichment mainly in the interleukin-17 (IL-17) and Toll-like receptor signaling pathways. (C) HP(2:10) was associated with greater new bone formation in rat calvarial defects at 4 and 8 weeks.

free control cultures.

Dexamethasone, sodium β-glycerophosphate, *L*-ascorbic acid (vitamin C), anhydrous ethanol, and dichloromethane were obtained from Macklin Biochemical Co., Ltd. (China). Dulbecco's Modified Eagle Medium (DMEM), fetal bovine serum (FBS), phosphate-buffered saline (PBS), trypsin, and TRIzol reagent were purchased from Thermo Fisher Scientific (United States of America [USA]). The penicillin–streptomycin solution used for macrophage culture was purchased from Gibco/Invitrogen (USA). The HiFiScript cDNA Synthesis Kit (CW2569M), UltraSYBR Mixture (Low ROX; CW2601M), and Ultrapure RNA Kit (CW0581M) were obtained from Cowin Biotech Co., Ltd. (China). Paraformaldehyde, radioimmunoprecipitation assay (RIPA) lysis buffer, ethylenediaminetetraacetic acid (EDTA), sodium citrate, hydrogen peroxide, bovine serum albumin (BSA), 4′,6-diamidino-2-phenylindole (DAPI), the BCA Protein Assay Kit (P0012), Cell Counting Kit-8 (CCK-8; C0042), the Live/Dead Cell Staining Kit (C2015S), the BCIP/NBT Alkaline Phosphatase Color Development Kit (C3206), and the Alkaline Phosphatase Assay Kit (P0321S) were purchased from Beyotime Biotechnology (China). Alkaline phosphatase (ALP) activity was measured using the *p*-nitrophenyl phosphate (p-NPP) method. Enzyme-linked immunosorbent assay (ELISA) kits for interleukin-10 (IL-10; EMC005) and IL-12 (EMC006) were purchased from NeoBioscience Technology Co., Ltd. (China). Primary antibodies against bone morphogenetic protein 2 (BMP-2; ab14933), vascular endothelial growth factor (VEGF; ab1316), CD163 (ab182422), and inducible nitric oxide synthase (iNOS; ab15323) were purchased from Abcam (USA). Alexa Fluor 488- (A-11008) and Alexa Fluor 594-conjugated (A-11012) secondary antibodies were purchased from Invitrogen/Thermo Fisher Scientific.

Scaffold fabrication and physicochemical characterization were performed using a 3D bioprinter (EFL-BP-6603, Suzhou Institute of Intelligent Manufacturing, China), a scanning electron microscope (Merlin, Carl Zeiss, Germany), a universal testing machine (34SC-5, Instron, USA), a contact angle goniometer (DSA25, Krüss GmbH, Germany), and a thermogravimetric analyzer (STA200, HITACHI, Japan). A vacuum oven (DZF-6020, Shanghai Yiheng Scientific Instruments Co., Ltd., China) was used to dry samples. Cell storage, culture, and scaffold sterilization involved a liquid nitrogen tank (3 L; Guangzhou Lithium Pavilion Technology Co., Ltd., China), a cell culture incubator

(MCO-18AIC, PHCbi, Japan), and a UV sterilizer (420 L; Shengzhiyuanhe Scientific and Educational Equipment Co., Ltd., China). Absorbance measurements were performed with a microplate reader (Spark, Tecan, Switzerland). RNA concentration was determined using a NanoDrop ONE spectrophotometer (Thermo Fisher Scientific), and reverse transcription was performed on a Mastercycler nexus thermal cycler (Eppendorf, Germany). Fluorescence images were acquired using an inverted fluorescence microscope (DMi8, Leica, Germany). Image analysis was performed using ImageJ software (National Institutes of Health, USA).

### 2.2. Preparation of HA/PCL scaffolds

Three scaffold formulations were prepared: pure PCL (P) and two nHA/PCL composites, designated HP(2:10) and HP(3:10). The composite formulations contained 0.2 and 0.3 g of nHA per 1 g of PCL, respectively, corresponding to nHA:PCL mass ratios of 2:10 and 3:10. The theoretical nHA fractions were 16.7 and 23.1 wt% of the total composite mass, respectively, whereas the P group contained no nHA. PCL (1 g) was dissolved in 20 mL of dichloromethane at room temperature under continuous magnetic stirring. For the composite groups, the specified amount of nHA was added to the polymer solution. Each mixture was then stirred continuously for 48 h to promote homogeneous nHA dispersion. The mixtures were cast into glass dishes and dried in a fume hood for 48 h, followed by vacuum drying at 40 °C for 72 h to remove residual dichloromethane. The resulting films were mechanically cut into small pellets measuring approximately 2 mm × 2 mm and loaded into the pneumatic extrusion cartridge of a 3D bioprinter. Scaffolds were printed in a 0°/90° lay-down pattern with a strand spacing of 800 μm and a layer height of 0.2 mm, giving a designed pore size of 400 μm × 400 μm. A 22-gauge nozzle with an inner diameter of 400 μm was used. The nozzle temperature was set to 70 °C–75 °C, and the platform temperature to 25 °C. Printing was performed at 300 mm/min under a pneumatic pressure of 0.45–0.52 MPa. All three groups used the same programmed toolpath and the printing parameters specified above to maintain scaffold architecture, including strand thickness, as consistently as possible across formulations.

### 2.3. Characterization and physico-chemical performance testing of scaffolds

#### *2.3.1. Surface morphology*

Scaffolds from each group were sputter-coated with gold, then examined for microscopic morphology and structure using scanning electron microscopy (SEM) at an accelerating voltage of 10 kV.[24]

#### *2.3.2. Determination of porosity*

Porosity was measured using the previously described ethanol immersion method.[24,25] Dried scaffolds measuring 7 mm in diameter and 1 mm in height were tested, with six specimens per group. Each scaffold was first weighed to obtain its dry mass ($M_0$). A specific gravity flask containing anhydrous ethanol was then weighed at room temperature ($M_1$). After a scaffold was immersed in the ethanol-filled flask, ultrasonication was applied for 10 min to ensure complete removal of trapped air bubbles, and the combined mass was measured ($M_2$). The scaffold was then removed, and the mass of the remaining ethanol in the flask was recorded ($M_3$). Porosity (%) was calculated using the following equation:

$$P(\%) = \frac{M_2 - M_3 - M_0}{M_1 - M_3} \times 100\% \quad (1)$$

The measurement results are expressed as the mean ± standard deviation.

#### *2.3.3. Mechanical strength test*

Scaffold specimens measuring 7 mm in diameter and 5 mm in height ($n$ = 6 per group) were rinsed three times with deionized water and vacuum-dried at 40 °C to constant mass. The specimens were then subjected to compression testing on a universal testing machine at a crosshead speed of 1 mm/min. The linear elastic portion of the resulting stress–strain curves was used to calculate the compressive modulus, following previously described methods.[24,26] Results are presented as the mean ± standard deviation.

#### *2.3.4. Hydrophilicity test*

Scaffold hydrophilicity was assessed by measuring apparent static water contact angles with a contact angle goniometer. Using the instrument's dispensing module, a 2 μL water droplet was slowly and uniformly deposited onto the top strut surface of each dried scaffold. Captured droplet images were analyzed with the instrument software, with the baseline adjusted to ensure measurement accuracy.[26-28] For each droplet, the contact angle was calculated as the arithmetic mean of the left and right angles:

$$\theta = (\theta_left + \theta_right)/2 \quad (2)$$

Measurements were performed at six randomly selected strut locations per group ($n$ = 6).

#### *2.3.5. Thermal weight loss data*

Thermal decomposition of the 3D-printed biomimetic scaffolds was examined using thermogravimetric analysis (TGA) under a nitrogen atmosphere, with samples heated from room temperature to 800 °C at a constant rate of 10 °C/min.[24]

## 2.4. Cellular experiments

### 2.4.1. Sterilization of cell culture and materials

Following retrieval from liquid-nitrogen storage and thawing, rBMSCs or RAW264.7 cells were cultured in DMEM supplemented with 10% FBS, 100 μg/mL penicillin, and 100 μg/mL streptomycin. Cultures were maintained at 37 °C in 5% $CO_2$, and only cells at passages 3–5 were used for the experiments.

Scaffolds from each group were immersed in 75% ethanol for 2 h and washed three times with sterile PBS before overnight sterilization in a UV sterilizer. Before cell experiments, three additional washes with sterile PBS were performed to remove residual washing solution.[24]

### 2.4.2. Biocompatibility evaluation of scaffolds

For the CCK-8 assay, rBMSCs were seeded at $1 \times 10^4$ cells per well in 48-well plates containing sterilized scaffolds, with cells cultured without scaffolds serving as the blank control (Con). Proliferation was evaluated on days 1, 4, and 7. At each time point, fresh medium supplemented with 10% (v/v) CCK-8 solution was added to replace the culture medium. Following incubation for 2 h at 37 °C in 5% $CO_2$, absorbance was recorded at 450 nm using a microplate reader.

For live/dead staining, scaffolds were seeded with rBMSCs at $1 \times 10^5$ cells per well and maintained in culture for 72 h. After three washes with PBS, the scaffolds were incubated in 0.5 mL of live/dead staining solution for 30 min at 37 °C in the dark. An inverted fluorescence microscope was used to visualize live cells in green and dead cells in red.

For SEM analysis, rBMSCs were cultured on the scaffolds for 72 h before fixation in 4% paraformaldehyde. Samples were subsequently dehydrated through an ethanol series of increasing concentrations (30%, 50%, 70%, 80%, 90%, 95%, and 99.5%), air-dried, and sputter-coated with gold. Cell morphology on the scaffolds was then examined using SEM at an accelerating voltage of 5 kV.

### 2.4.3. In vitro osteogenic differentiation evaluation of rBMSCs

rBMSCs at passages 3–5 were seeded at $1 \times 10^5$ cells per well onto sterilized 3D-printed scaffolds (P, HP[2:10], and HP[3:10]) in 48-well plates to assess osteogenic responses under induction conditions. Cells seeded directly onto TCPS wells without scaffolds served as the control (Con). Following an initial attachment period of 24 h, the culture medium in all groups was replaced with osteogenic induction medium (OIM). OIM comprised complete DMEM supplemented with 10 mM β-glycerophosphate, 100 nM dexamethasone, and 50 μg/mL *L*-ascorbic acid, and was renewed every 2–3 days. Since all groups received identical exogenous osteogenic stimuli, the results reflect relative differences in cellular osteogenic responses to the scaffolds under induction conditions.

On day 7 of osteogenic induction, ALP staining and activity measurements were performed in the P, HP(2:10), and HP(3:10) scaffold groups. For staining, rBMSCs were fixed in 4% paraformaldehyde and processed with a BCIP/NBT Alkaline Phosphatase Color Development Kit following the manufacturer's instructions. For quantitative analysis, cells were lysed in RIPA buffer without protease inhibitors. ALP activity in the lysates was measured with an Alkaline Phosphatase Assay Kit based on the p-NPP method, while total protein concentration was determined with a BCA Protein Assay Kit. The measured ALP activity was normalized to total protein content and reported as U/mg protein.

Total RNA was extracted from rBMSCs at days 7 and 14 of osteogenic induction using TRIzol reagent and reverse-transcribed into complementary DNA using the HiFiScript cDNA Synthesis Kit. Reverse transcription quantitative polymerase chain reaction (RT-qPCR) was performed using Ultra SYBR Mixture (Low ROX) to examine the expression of the osteogenic genes *Alp*, *Runx2*, *Col1*, *Bmp2*, and *Opn*, with rat *Gapdh* as the endogenous reference gene. Relative transcript levels were calculated using the $2^{-\Delta\Delta Ct}$ method. For each gene at each time point, the group with the lowest expression was set to 1.0 to illustrate relative fold changes among groups; because the calibrator group differs between genes and time points, fold changes are interpretable only within the same gene and time point, and not across genes or between day 7 and day 14. Each experiment included six independent biological replicates ($n$ = 6; independent culture wells), each measured in technical triplicate. The rat-specific primer sequences are listed in Table 1.

### 2.4.4. Performance evaluation of scaffolds for macrophage polarization

For macrophage culture and polarization assay, RAW264.7 macrophages were cultured at 37 °C in 5% $CO_2$ in DMEM containing 10% FBS and 1% penicillin–streptomycin. Sterilized P, HP(2:10), and HP(3:10) scaffolds were placed in 48-well plates and seeded with $5 \times 10^4$ cells per well. Cells cultured without scaffolds served as the blank control (Con).

Total RNA was isolated on days 1 and 3 with the Ultrapure RNA Kit following the manufacturer's instructions, and RNA concentration was determined using a spectrophotometer. For each sample, 1 μg of

RNA was reverse-transcribed with the HiFiScript cDNA Synthesis Kit using a thermal cycler. Expression of the M1 marker *Il1b* and the M2 marker *Cd206* was quantified using RT-qPCR with UltraSYBR Mixture (Low ROX), with *Gapdh* as the reference gene. Primer sequences are provided in Table 1. Relative expression levels were calculated by the $2^{-\Delta\Delta Ct}$ method, with the lowest-expressing group for each gene at each time point assigned a value of 1.

For cytokine measurement, culture supernatants were collected on days 1 and 3, and the concentrations of IL-12 and IL-10 were determined using ELISA kits according to the manufacturer's instructions. Absorbance at 450 nm was measured with a Spark microplate reader, and concentrations were calculated from standard curves.

#### *2.4.5. RNA sequencing*

RAW264.7 cells were cultured for 3 d in 6-well plates containing sterile 3D-printed HP(2:10) scaffolds or no scaffolds as the blank control (Con). Three biological replicates were included in each group. Total RNA was extracted with TRIzol reagent, and fragmented messenger RNA was used to prepare libraries with the Hieff NGS® Ultima Dual-mode mRNA Library Prep Kit (12309ES, Yeasen, China). Sequencing was conducted on an Illumina NovaSeq 6000 platform (Illumina, USA).

Raw reads underwent adapter trimming and low-quality read removal with fastp (v0.18.0). The resulting clean reads were mapped to the Ensembl release 111 mouse reference genome with HISAT2 (v2.1.0). Reference-based transcript assembly was subsequently performed with StringTie (v1.3.4d), and gene abundances were quantified with RSEM (v1.2.19). Unnormalized integer read count matrices served as input for differential expression analysis using the DESeq2 package (v1.24.0).[29] For exploratory profiling, candidate differentially expressed genes (DEGs) were screened using an unadjusted $p$-value < 0.05 and an absolute fold change ≥ 1.5 ($|\log_2 FC| \geq 0.585$). Benjamini–Hochberg false discovery rates (FDR/adjusted $p$-value [padj]) were also calculated, and genes with padj < 0.05 were identified as FDR-significant. Complete differential expression statistics are provided in Table S1.

The candidate DEGs were subjected to functional enrichment analysis using the Kyoto Encyclopedia of Genes and Genomes (KEGG)[30-32] and Gene Ontology (GO) databases. GO analysis encompassed the biological process (BP), cellular component (CC), and molecular function (MF) categories. For both KEGG and GO analyses, multiple-testing correction was applied at the pathway or term level ($Q$ value); however, this correction does not account for the selection of candidate DEGs based on unadjusted $p$-values. A volcano plot illustrated the distribution of candidate DEGs, while a chord diagram displayed the relationships between selected DEGs and KEGG pathways. The RNA-seq datasets generated in this study have been deposited in the Gene Expression Omnibus (GEO, https://www.ncbi.nlm.nih.gov/geo) under accession number GSE302053.

### 2.5. Experiments *in vivo*

#### *2.5.1. Implantation of scaffolds in vivo*

Approval for all animal experiments was granted by the Laboratory Animal Welfare and Ethics Committee of the Institute of Biology and Medical Engineering, Guangdong Academy of Sciences (No. 2024021), and the experiments were conducted in accordance with the ARRIVE guidelines 2.0. Forty-eight male Sprague-Dawley rats, aged 8 weeks and weighing 200–220 g, were obtained from the Guangdong Quality Supervision and Inspection Station

**Table 1. Sequences of primers used in real-time quantification of selected genes**

| Gene transcript | Forward primer sequence (5'–3') | Reverse primer sequence (5'–3') |
|---|---|---|
| *Gapdh* | GCCATGAGGTCCACCACCCT | AAGGTCATCCCAGAGCTG |
| *Alp* | GGAGATGGTATGGGCGTCTC | GGACCTGAGCGTTGGTGTTA |
| *Bmp-2* | ACCCGCTGTCTTCTAGTGTTG | TTCTTCGTGATGGAAGCTGAG |
| *Col1* | TTCTCCTGGCAAAGACGGAC | CTCAAGGTCACGGTCACGAA |
| *Opn* | TGAAACTCGTGGCTCTGATG | GATGAACCAAGCGTGGAAAC |
| *Runx2* | TCGGAGAGGTACCAGATGGG | AGGTGAAACTCTTGCCTCGT |
| *IL-1β* | TACAGGCTCCGAGATGAACA | AGGCCACAGGTATTTTGTCG |
| *Cd206* | ATGGATGTTGATGGCTACTGG | TTCTGACTCTGGACACTTGC |

of Medical and Healthcare Devices (China). Animals were housed in groups of three per cage at 20 °C–22 °C on a 12-h light/12-h dark cycle, with unrestricted access to sterile standard diet and water. A seven-day acclimatization period preceded surgery.

A computer-generated random sequence was used to assign the rats to four groups of 12 animals: blank control (Con; empty defects), P scaffold, HP(2:10) scaffold, and HP(3:10) scaffold. Within each group, six animals were assigned to each of the two endpoints, 4 and 8 weeks. Each animal received a coded identifier, and treatment allocation remained concealed until surgery. Personnel responsible for micro-computed tomography (CT) scanning, histological staining, image acquisition, and quantification were blinded to group allocation.

General anesthesia was induced with an intraperitoneal injection of sodium pentobarbital (40 mg/kg). Following shaving and disinfection, the calvarium was exposed through an approximately 1.5 cm longitudinal incision along the sagittal suture. A motorized trephine bur was used to create two symmetrical critical-sized cylindrical defects, each 5 mm in diameter, with one defect on either side of the parietal bone. Continuous irrigation with sterile saline was applied during drilling to prevent thermal necrosis.[32] Both defects within an animal received the same assigned treatment. In the scaffold groups, sterile, cell-free scaffolds measuring 5 mm in diameter and 1 mm in thickness were implanted directly, without pre-incubation or cell seeding; defects in the Con group were left empty. The periosteum and skin were then repositioned and sutured in layers.

Postoperative analgesia consisted of subcutaneous meloxicam at 1 mg/kg/day for three consecutive days. At the designated 4- or 8-week endpoint, animals were euthanized with an intraperitoneal injection of a lethal dose of pentobarbital sodium (150 mg/kg), in accordance with the AVMA Guidelines for the Euthanasia of Animals (2020 Edition). The calvaria were subsequently harvested.

#### *2.5.2. Micro-computed tomography analysis*

Images were reconstructed with an isotropic voxel size of 10.0 μm and analyzed using CTAn software (v1.18, Bruker, USA). A cylindrical volume of interest (VOI), 5.0 mm in diameter and 1.0 mm in height, was centered on the original calvarial defect. Bone mineral density (BMD) was calibrated using hydroxyapatite (HA) phantoms with known densities of 0.25 and 0.75 g/cm$^3$. A lower density threshold of 400 mg HA/cm$^3$ was used to segment mineralized tissue. Baseline scans of unimplanted scaffolds showed apparent densities below 200 mg HA/cm$^3$, supporting the use of this threshold to distinguish mineralized tissue from scaffold background. Bone volume fraction (BV/TV) and mean BMD were calculated within the VOI. Measurements from the bilateral defects were averaged to obtain one value per animal.

#### *2.5.3. Histological analysis*

After micro-CT analysis, specimens underwent decalcification in 10% EDTA solution for 1 month, followed by paraffin embedding and sectioning at a thickness of 5 μm. Tissue morphology and new bone formation were evaluated using hematoxylin and eosin (H&E) staining, while collagen deposition was examined using Masson's trichrome staining.

For immunofluorescence staining, deparaffinized and rehydrated sections underwent heat-induced antigen retrieval in 10 mM sodium citrate buffer (pH 6.0) for 15 min at 95 °C. Endogenous peroxidase activity was quenched with 3% (w/v) hydrogen peroxide, after which sections were blocked in PBS containing 3% (w/v) BSA for 1 h at room temperature. Primary antibodies against BMP-2 (1:200), VEGF (1:200), and CD163 (1:2,000), or iNOS (1:1,000), were applied overnight at 4 °C. Following thorough PBS washing, sections were incubated with Alexa Fluor 488- and Alexa Fluor 594-conjugated secondary antibodies (1:500) for 1 h at room temperature in the dark. DAPI was used for nuclear counterstaining.

Fluorescence images were captured with an inverted fluorescence microscope, using identical exposure settings for all images within each stain. Image analysis was performed in ImageJ. For Masson's trichrome staining, the blue collagen channel was isolated through color deconvolution. A fixed threshold was then applied, and collagen area was expressed as a percentage of the total tissue area within the defect. For immunofluorescence, individual channels were separated to measure the positive-staining area and mean fluorescence intensity of BMP-2, VEGF, CD163, and iNOS within the defect region. Positive-staining area was defined as the percentage of the analyzed area with signal above a fixed threshold.

Six randomly selected, non-overlapping fields were analyzed for each animal, and their measurements were averaged to yield a single value per animal. For each marker at each time point, fluorescence intensity was normalized to the mean intensity of the group with the lowest fluorescence intensity, which was assigned a value of 1. All measurements were quantified by an observer blinded to group allocation.

### 2.6. Statistical analysis

Quantitative results are expressed as the mean ± standard deviation (SD). Unless otherwise specified, *in vitro* experiments included six independent biological replicates,

defined as distinct culture wells or independently prepared scaffolds. Where applicable, measurements were performed in technical triplicate for each biological replicate, and the three technical values were averaged before statistical analysis. For *in vivo* experiments, six animals were included per group at each time point, with $n$ denoting the number of animals. Measurements from the bilateral defects or six randomly selected fields within each animal were averaged to generate a single value per animal. RNA-seq included three biological replicates per group.

Statistical analyses were conducted in GraphPad Prism 9 (GraphPad Software, LLC, USA). Differences among more than two groups at a single time point were evaluated by one-way analysis of variance (ANOVA) followed by Tukey's post hoc test. Analyses involving group and time as the two factors were performed using two-way ANOVA with Sidak's multiple comparisons test. RNA-seq differential expression analysis was conducted using DESeq2, with candidate DEGs defined by an unadjusted $p < 0.05$ and $|\log_2 FC| \geq 0.585$ ($|\text{fold change}| \geq 1.5$), alongside Benjamini–Hochberg FDR reporting in Table S2. Statistical significance was defined as a two-sided $p < 0.05$, with significance levels indicated as $^{*}p < 0.05$, $^{**}p < 0.01$, and $^{***}p < 0.001$.

## 3. Results

### 3.1. Surface morphology and physicochemical properties of scaffolds

Because the physical properties of scaffolds critically affect cell behavior, we characterized the morphology, thermal stability, hydrophilicity, porosity, and compressive properties of the three scaffold groups. As shown in Figure 2A, all scaffolds exhibited interconnected orthogonal macropores (>300 μm), with comparable average strut diameters (390–400 μm) and pore sizes (350–360 μm, $p > 0.05$). High-magnification SEM revealed nodular features and micro-voids on pure PCL, which may be related to spherulitic crystallization and thermal contraction of the polymer during cooling on the 25 °C platform. Because the nozzle temperature (70 °C–75 °C) exceeded the melting range of PCL, incomplete melting appears less likely, but printing-related contributions cannot be excluded in the absence of direct evidence such as crystallinity or thermal analysis. The denser strut surfaces observed after nHA incorporation may reflect heterogeneous nucleation and micro-pore filling. TGA up to 800 °C showed that the residual mass of the HP(2:10) and HP(3:10) groups was 13.7% and 21.2%, respectively, consistent with theoretical inorganic loadings (16.7 wt% and 23.1 wt%) considering the 3%–6% lattice dehydroxylation and moisture loss of synthetic nHA (Figure 2B).[33] The composite scaffolds exhibited lower apparent water contact angles than the P scaffold, and the contact angle decreased with increasing nHA content, with the lowest value in the HP(3:10) group (Figure 2C and 2D). This trend is compatible with the hydrophilic hydroxyl groups on the nHA surface.[34] However, because the angles were measured directly on porous printed struts, the contribution of surface chemistry cannot be separated from that of surface roughness and geometry. A lower apparent contact angle has been associated with better cell adhesion and attenuated immune responses.[35] Porosity was approximately 65% in all groups, with no significant differences among them (Figure 2E). The compressive strength of the HP(2:10) group was higher than that of the P and HP(3:10) groups (Figure 2F, Figure S1), a non-monotonic dependence on the ceramic content that has also been reported for PCL/HA scaffolds,[36] whereas the compressive modulus of the HP(3:10) group was higher than that of the HP(2:10) group (Figure 2G, Figure S1), in line with the non-monotonic change of modulus with nHA content in PCL–nHA composites.[33]

### 3.2. Biocompatibility evaluation of scaffolds

Good biocompatibility is essential for implantable biomaterials. The proliferation and adhesion of rBMSCs were evaluated using CCK-8 assays after culture for 1, 4, and 7 days, and using live/dead staining and SEM after 72 h of culture. The optical density (OD) values increased with culture time in all groups (Figure 3A), indicating that none of the scaffolds prevented cell growth. The HP(2:10) group showed the highest OD values among the four groups at all time points, and was significantly higher than the HP(3:10) group at days 1 and 7. In contrast, the HP(3:10) group did not show a further increase in proliferation compared with the P and Con groups.

Live/Dead staining (Figure 3B) was consistent with the CCK-8 results. Numerous live (green) cells were observed on the HP(2:10) scaffolds, whereas fewer live cells and more red-stained cells were observed on the HP(3:10) scaffolds. SEM images (Figure 3C) further showed differences in cell coverage of the strut surface. Many open micropores remained exposed on the strut surfaces of the P and HP(3:10) scaffolds (dashed circles), whereas the strut surface of the HP(2:10) scaffold was covered by a confluent, continuous cell layer that bridged and overlaid the underlying micropores (arrows). The reduced proliferation and coverage on the HP(3:10) scaffolds relative to HP(2:10) may be related to concentration-dependent cellular stress at the higher nHA loading[12], although this was not directly examined in the present study. Overall, the HP(2:10) scaffold exhibited the most favorable cytocompatibility among the formulations tested, as reflected by greater rBMSC proliferation and more extensive cell coverage.

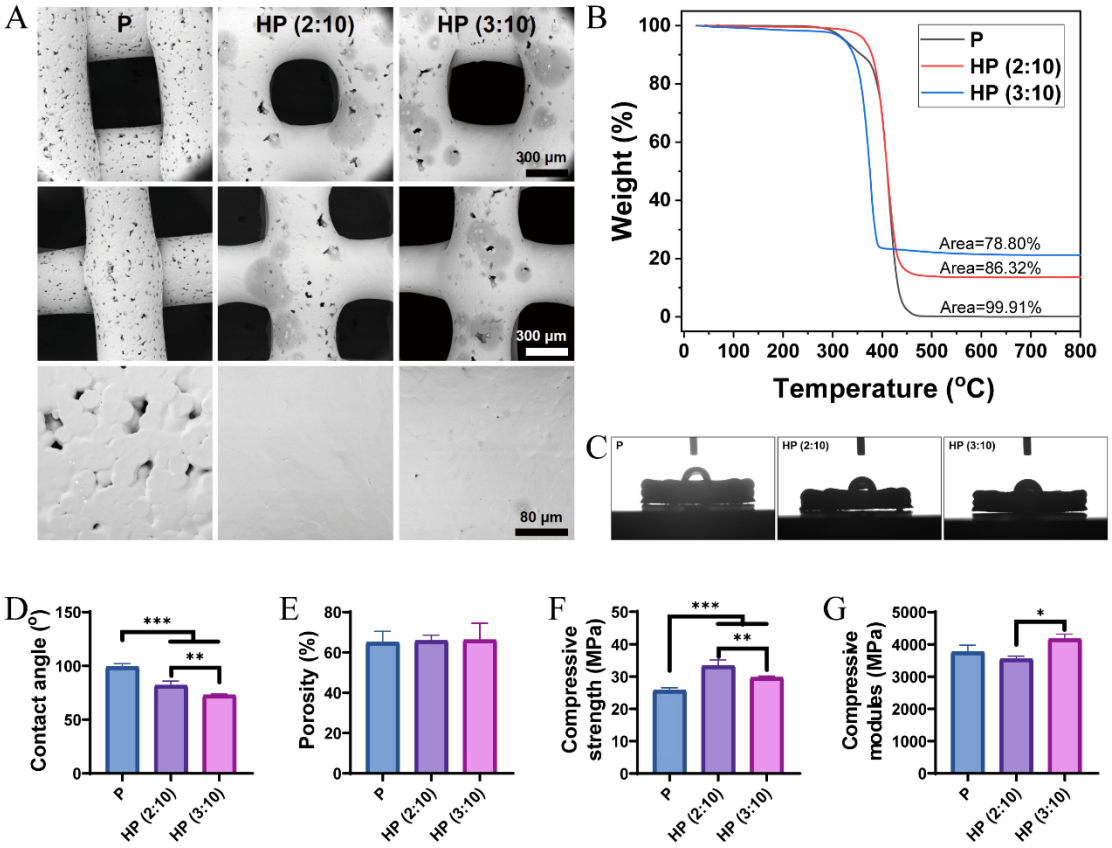



**Figure 2.** Physicochemical properties of P, HP(2:10), and HP(3:10) scaffolds. (A) Scanning electron microscopy (SEM) images at low (200×) and high (1000×) magnification, with the top and middle rows showing low magnification and the bottom row showing high magnification. Scale bars: 300 μm for the top and middle rows, and 80 μm for the bottom row. (B) Thermogravimetric analysis (TGA) curves recorded under nitrogen, with labels indicating weight loss at 800 °C. (C) Representative water droplet images and (D) corresponding apparent static contact angles. Each droplet angle was calculated as the mean of the left and right angles. (E) Scaffold porosity measured through ethanol immersion. (F) Compressive strength. (G) Compressive modulus. Notes: Quantitative data in D–G are expressed as mean ± SD. Contact angles were measured at six randomly selected strut locations per group (D); porosity and compressive properties were assessed using six scaffold specimens per group (E–G). Statistical comparisons were performed using one-way ANOVA followed by Tukey's post hoc test. *$p < 0.05$, **$p < 0.01$, ***$p < 0.001$. P: Pure polycaprolactone (PCL) scaffold; HP(2:10) and HP(3:10): Nano-hydroxyapatite (nHA)/PCL composite scaffolds with nHA:PCL mass ratios of 2:10 and 3:10, corresponding to theoretical nHA contents of 16.7 and 23.1 wt%, respectively.

### 3.3. Osteogenic performance evaluation of scaffolds *in vitro*

Osteogenic responses were examined in rBMSCs cultured under osteogenic induction conditions for up to 14 days on P, HP(2:10), and HP(3:10) scaffolds, with scaffold-free cultures serving as the control (Con). Assessments included ALP staining and activity on day 7 and RT-qPCR analysis of *Alp*, *Col1*, *Bmp2*, Runx2, and *Opn* expression on days 7 and 14.

On day 7, ALP-positive staining was more pronounced on P and HP(2:10) than on HP(3:10) scaffolds (Figure 4A). ALP activity reached 9.2 U/mg protein in HP(2:10), exceeding the values measured in P (6.1 U/mg protein) and HP(3:10) (6.4 U/mg protein; both $p < 0.05$). No significant difference in ALP activity was observed between P and HP(3:10) (Figure 4A).

At day 7 (Figure 4B), relative *Alp* expression in HP(2:10) was 3.0-fold and exceeded that in P ($p < 0.05$). *Col1* and *Runx2* reached 3.6- and 4.4-fold, respectively, in HP(2:10), with both genes expressed at higher levels than in all three other groups. For *Col1*, the differences were significant relative to Con ($p < 0.001$), P, and HP(3:10) (both $p < 0.05$); for *Runx2*, significance was observed relative to Con ($p < 0.05$), P, and HP(3:10) (both $p < 0.01$). *Opn* expression in HP(2:10) was 4.3-fold higher than in Con and HP(3:10) (both $p < 0.01$). The highest *Bmp2* expression was also recorded in HP(2:10), at 4.9-fold.

At day 14 (Figure 4C), expression levels of *Alp*, *Col1*,

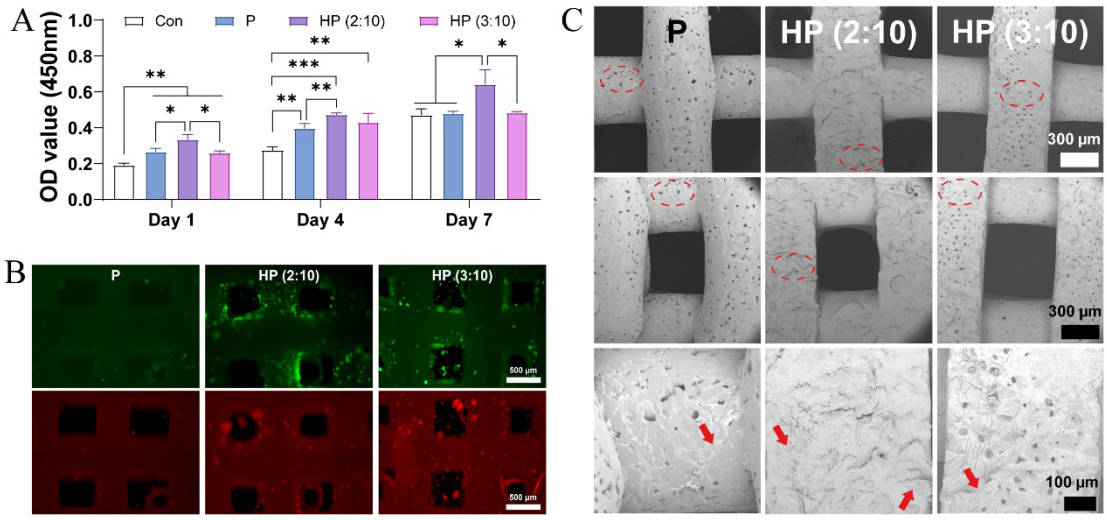



**Figure 3.** Rat bone marrow mesenchymal stem cell (rBMSC) proliferation and adhesion on the scaffolds. (A) Cell Counting Kit-8 (CCK-8) measurements after 1, 4, and 7 days of culture, expressed as optical density (OD) at 450 nm. (B) Live/Dead fluorescence images at 72 h, with viable cells shown in green and dead cells in red. Scale bar: 500 μm; magnification: 5×. (C) Scanning electron microscopy images of scaffold-associated rBMSCs at 72 h; low (200×, top and middle rows) and high (1000×, bottom row) magnification. Scale bars: 300 μm for the upper and middle rows, and 100 μm for the lower row. Red dashed circles mark open micropores on the strut surface, while red arrows identify the covering cell layer. Unannotated images are provided in Figure S2. Notes: Data in A are expressed as mean ± SD (n = 6 independent biological replicates) and were analyzed using two-way ANOVA with group and culture time as factors, followed by Sidak's multiple comparisons test. *$p < 0.05$, **$p < 0.01$, ***$p < 0.001$. Con: Cells cultured without scaffolds; P: Pure polycaprolactone (PCL) scaffold; HP(2:10) and HP(3:10): Nano-hydroxyapatite (nHA)/PCL composite scaffolds with nHA:PCL mass ratios of 2:10 and 3:10, respectively.

*Opn*, *Bmp2*, and *Runx2* in HP(2:10) were 7.8, 9.9, 10.0, 6.4, and 4.7 times higher than those in Con, respectively. HP(2:10) also showed higher expression of *Alp*, *Col1*, *Opn*, and *Bmp2* than both P and HP(3:10) (all $p < 0.001$). *Runx2* expression exceeded that in Con ($p < 0.01$) and HP(3:10) ($p < 0.001$). By contrast, neither *Col1* nor *Opn* expression in HP(3:10) differed significantly from that in Con or P.

Overall, HP(2:10) supported higher ALP activity and a generally stronger osteogenic gene expression response in rBMSCs than P and HP(3:10) under osteogenic induction conditions.

### 3.4. Evaluation of scaffold-promoted Macrophage polarization properties and RNA sequencing

To assess the immunomodulatory effects of the scaffolds, RAW264.7 macrophages were cultured on the P, HP(2:10), and HP(3:10) scaffolds, and the expression of the M1 marker *Il1b* and the M2 marker *Cd206* was measured using RT-qPCR at days 1 and 3 (Figure 5A and 5B). *Il1b* expression was lowest in the HP(2:10) group at both time points, whereas *Cd206* expression was highest in the HP(2:10) group. The levels of IL-12 and IL-10 in the culture supernatants were measured using ELISA (Figure 5C and 5D): IL-12 was lowest, and IL-10 was highest in the HP(2:10) group at both time points. Together, these results indicate that the HP(2:10) scaffold promoted an M2-like and suppressed an M1-like marker profile more strongly than the P and HP(3:10) scaffolds under the conditions tested. Because only a limited set of markers was assessed, these data describe a shift in marker expression and cytokine secretion rather than a complete characterization of macrophage polarization.

To explore candidate transcriptomic responses associated with the scaffolds, RNA-seq was performed on RAW264.7 cells in the Con and HP(2:10) groups after three days of culture (Figure 6). Compared with the Con group, 136 candidate DEGs were identified in the HP(2:10) group, of which 16 were upregulated and 120 were downregulated, and 38 of these remained significant after Benjamini–Hochberg correction (padj < 0.05) (Figure 6A and 6B; Table S2). GO annotation indicated that the candidate DEGs were mainly associated with biological processes related to immune and inflammatory responses (Figure 6D). KEGG pathway enrichment analysis showed that the IL-17 ($Q = 0.006$) and Toll-like receptor ($Q = 0.015$) signaling pathways were enriched at a pathway-level FDR of $Q < 0.05$, whereas the tumor necrosis factor (TNF), cyclic AMP (cAMP), T-helper 1 (Th1)/Th2 cell differentiation, and nuclear factor kappa B (NF-κB) pathways showed only nominal enrichment ($Q \geq 0.05$) (Figure 6C; Table S3).

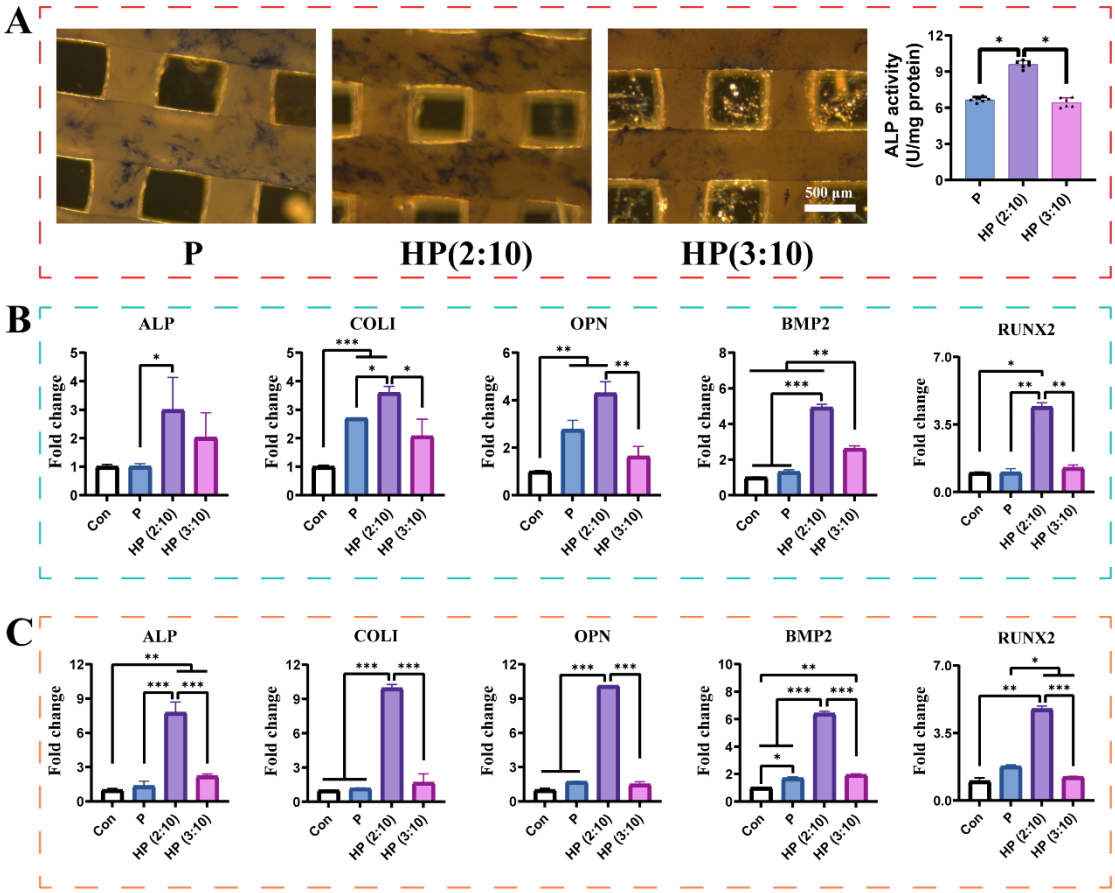



**Figure 4.** Osteogenic responses of rat bone marrow mesenchymal stem cells (rBMSCs) to the scaffolds under osteogenic induction conditions. (A) BCIP/nitro blue tetrazolium (NBT) staining and protein-normalized alkaline phosphatase (ALP) activity (U/mg protein) in P, HP(2:10), and HP(3:10) cultures on day 7. Scale bar: 500 μm; magnification: 5×. (B, C) Reverse transcription quantitative polymerase chain reaction (RT-qPCR) measurements of *Alp*, *Col1*, *Opn*, *Bmp2*, and *Runx2* expression on days (B) 7 and (C) 14. Transcript levels were normalized to *Gapdh*, with the lowest-expressing group for each gene at each time point assigned a value of 1. Relative expression values are intended for comparisons among groups within the same gene and time point, not across genes or time points.

Notes: Quantitative data are expressed as mean ± SD ($n$ = 6 independent biological replicates). ALP activity in A was analyzed by one-way ANOVA followed by Tukey's post hoc test; gene expression data in B and C were analyzed by two-way ANOVA with Sidak's multiple comparisons test. *$p < 0.05$, **$p < 0.01$, ***$p < 0.001$. Con: rBMSCs cultured on tissue culture polystyrene (TCPS) without scaffolds; P: Pure polycaprolactone (PCL) scaffold; HP(2:10) and HP(3:10): Nano-hydroxyapatite (nHA)/PCL composite scaffolds with nHA:PCL mass ratios of 2:10 and 3:10, respectively.

Chord analysis showed that the candidate DEGs mapped to these pathways included *Fos*, *Fosl1*, *Jund*, *Ptgs2*, *Csf2*, *Tlr9*, *Mmp9*, *Spp1*, *Ccl3*, and *Ccl4*, several of which were shared among pathways (Figure 6E). Among them, *Fos*, *Jund*, and *Tlr9* were downregulated, whereas *Mmp9*, *Spp1*, *Ccl3*, and *Ccl4* were moderately upregulated in the HP(2:10) group (Table S2). Taken together, these data describe a transcriptional profile of macrophages cultured with HP(2:10) and provide preliminary candidate hypotheses for future investigation. Functional validation of selected transcripts will be needed to determine whether these expression changes translate into altered pathway activity.

### 3.5. HP(2:10) scaffold is associated with improved bone regeneration in rat calvarial defects

Bone regeneration and the local immune microenvironment were evaluated at 4 and 8 weeks in a critical-sized rat calvarial defect model using micro-CT, H&E, Masson's trichrome, and immunofluorescence staining. Defects received P, HP(2:10), or HP(3:10) scaffolds, while those left empty served as the control (Con).

Micro-CT reconstructions revealed distinct patterns of bone formation among the groups (Figure 7A). HP(2:10) showed elongated, strip-like new bone at 4 weeks and

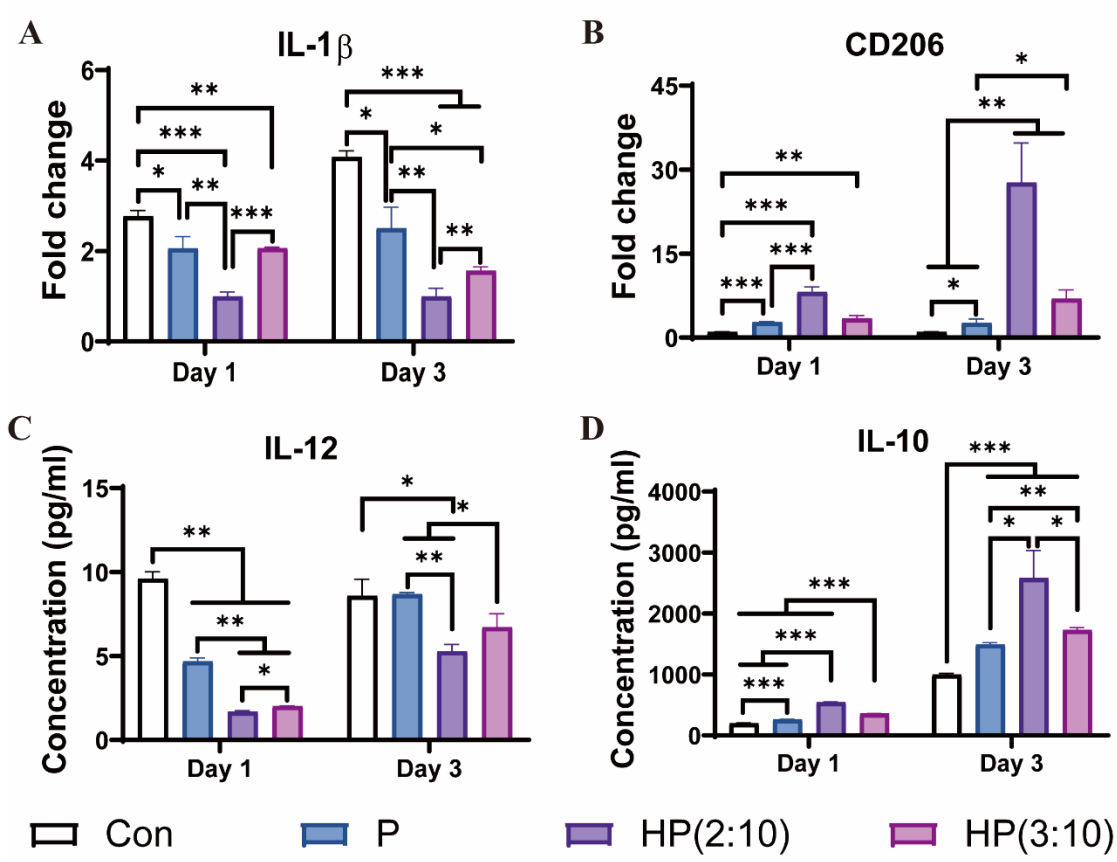



**Figure 5.** Inflammation-related gene expression and cytokine secretion in RAW264.7 macrophages cultured on the scaffolds. (A, B) Reverse transcription quantitative polymerase chain reaction (RT-qPCR) analysis of (A) the M1-associated marker *Il1b* and (B) the M2-associated marker *Cd206* after 1 and 3 days of culture. Transcript levels were normalized to *Gapdh*, with the lowest-expressing group for each gene at each time point assigned a value of 1. Relative expression values are intended for comparisons among groups within the same gene and time point. (C) Interleukin-12 (IL-12) and (D) IL-10 concentrations in culture supernatants collected on days 1 and 3, determined using enzyme-linked immunosorbent assay (ELISA).
Notes: Data are expressed as mean ± SD ($n = 6$ independent biological replicates). Statistical comparisons were performed using two-way ANOVA followed by Sidak's multiple comparisons test. *$p < 0.05$, **$p < 0.01$, ***$p < 0.001$. Con: RAW264.7 cells cultured without scaffolds; P: Pure polycaprolactone (PCL) scaffold; HP(2:10) and HP(3:10): Nano-hydroxyapatite (nHA)/PCL composite scaffolds with nHA:PCL mass ratios of 2:10 and 3:10, respectively.

multiple bone strands extending across the defect at 8 weeks. By comparison, Con defects remained largely unfilled at both time points, with only a few thin bone fragments. Small, isolated bone nodules were observed in P, with several nodules present at 8 weeks. In HP(3:10), scattered granular bone fragments at 4 weeks were followed by multiple isolated bone nodules at 8 weeks.

The BMD measurements supported the imaging observations (Figure 7B). At 4 weeks, BMD reached 0.22 g/cm$^3$ in HP(2:10), compared with 0.15 g/cm$^3$ in Con ($p < 0.001$) and 0.18 g/cm$^3$ in P ($p < 0.05$). At 8 weeks, HP(2:10) had a BMD of 0.30 g/cm$^3$, exceeding Con (0.16 g/cm$^3$), P (0.22 g/cm$^3$), and HP(3:10) (0.24 g/cm$^3$) (all $p < 0.01$). BV/TV was also higher in HP(2:10), reaching 15.4% at 4 weeks and 20.8% at 8 weeks (Figure 7C). Corresponding values were 4.8% and 9.5% in Con, 10.2% and 13.0% in P, and 11.4% and 16.3% in HP(3:10). At both time points, HP(2:10) exceeded Con and P (all $p < 0.001$) and HP(3:10) (both $p < 0.01$). P also showed higher BV/TV than Con at 4 weeks ($p < 0.001$) and 8 weeks ($p < 0.01$). Across all groups, BMD and BV/TV values were higher at 8 weeks than at 4 weeks.

We examined tissue morphology within the defect region at 4 and 8 weeks after implantation using H&E staining (Figure 8). In the Con group, the defect was occupied by thin, loosely arranged fibrous tissue at both time points. In the P group, the scaffold pores contained loose fibrous connective tissue with blood vessels at 4 weeks, and fibrous tissue with erythrocytes at 8 weeks. In the HP(2:10) group, a nodular matrix surrounded

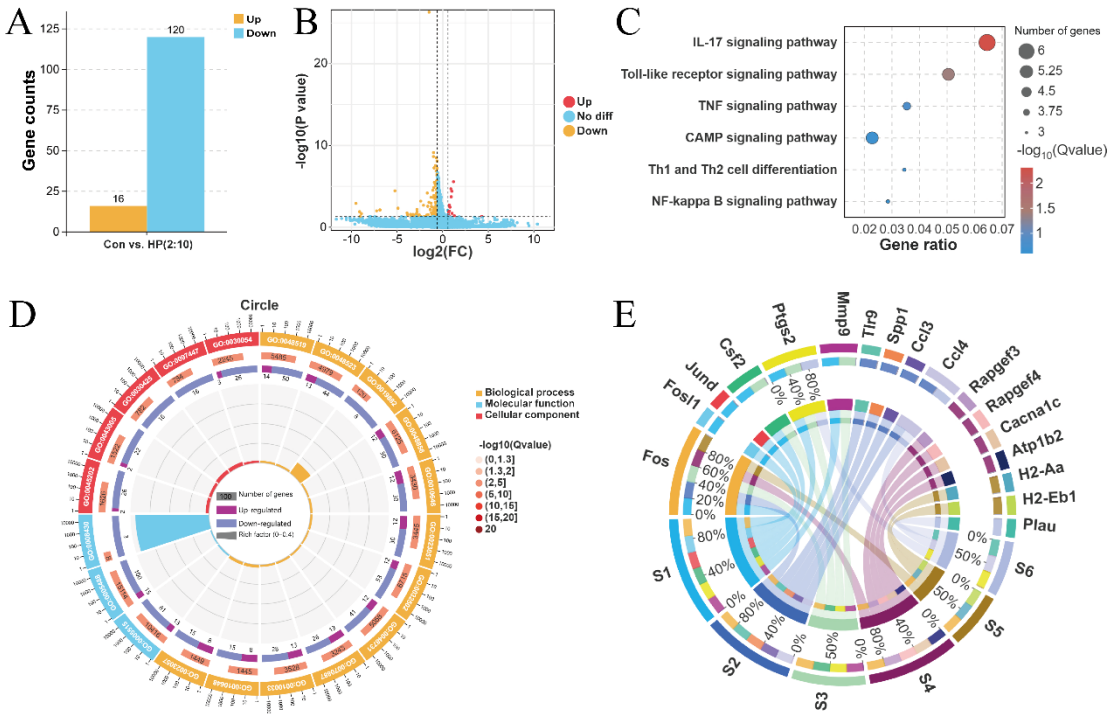



**Figure 6.** Exploratory transcriptomic comparison of RAW264.7 macrophages cultured with HP(2:10) scaffolds and scaffold-free controls (Con) for three days. (A) Candidate differentially expressed gene (DEG) counts between the Con and HP(2:10) groups (16 upregulated and 120 downregulated). (B) Volcano plot showing differential gene expression. Red, orange, and cyan dots denote upregulated, downregulated, and non-significant genes, respectively. (C) Kyoto Encyclopedia of Genes and Genomes (KEGG) pathway enrichment bubble plot of the candidate DEGs, where *Q* values represent pathway-level false discovery rate correction. Bubble size indicates gene number, and color represents $-\log_{10}(Q \text{ value})$. Pathways are arranged from top to bottom as follows: interleukin-17 (IL-17) signaling (S1), Toll-like receptor signaling (S2), tumor necrosis factor (TNF) signaling (S3), cyclic AMP (cAMP) signaling (S4), T-helper 1 (Th1) and Th2 cell differentiation (S5), and nuclear factor kappa B (NF-κB) signaling (S6). (D) Gene Ontology (GO) enrichment circle plot encompassing biological process, molecular function, and cellular component terms; color indicates $-\log_{10}(Q \text{ value})$, and bar length represents gene number. (E) Chord diagram showing the relationships between selected candidate DEGs and KEGG pathways S1–S6; the direction of change is provided in Table S2. Candidate DEGs were screened by unadjusted $p < 0.05$ and $|\log_2 FC| \geq 0.585$ ($|\text{fold change}| \geq 1.5$); following Benjamini–Hochberg correction (padj < 0.05), 38 of these candidate DEGs remained significant (Table S2). Three biological replicates were included per group.

by cells was observed within the pore region at 4 weeks. At 8 weeks, a dense eosinophilic matrix containing cells within lacunae-like spaces was evident, consistent with newly formed bone. In the HP(3:10) group, the pores were predominantly filled with fibrous tissue at both time points. These findings were qualitative.

Masson's trichrome staining showed sparse collagen (blue) in the Con group and more collagen in the scaffold groups (Figure 9A). In the HP(2:10) group, dense blue collagen surrounded the nodular matrix at 4 weeks, and the densely stained area was larger at 8 weeks. The collagen area fraction in the HP(2:10) group (28.8% at 4 weeks and 37.0% at 8 weeks) was larger than that in the Con group (7.5% and 21.0%), the P group (17.0% and 25.0%), and the HP(3:10) group (23.0% and 29.0%) (all $p < 0.001$; Figure 9B and 9C).

Immunofluorescence staining for VEGF and BMP-2 was performed to assess the expression of angiogenesis- and osteogenesis-related factors in the defect area at 4 and 8 weeks after implantation (Figure 10A and 10B). Signals for both markers were weak in the Con group at both time points, whereas stronger signals were observed in the scaffold groups, with the HP(2:10) group showing the most extensive staining (Figure 10A and 10B). Quantitative analysis showed that the VEGF-positive area in the HP(2:10) group (7.0% at 4 weeks and 12.9% at 8 weeks) was larger than that in the Con group (1.1% and 1.5%), the P group (2.4% and 7.6%), and the HP(3:10) group (4.6% and 10.8%) (all $p < 0.001$; Figure 10C and 10D). The relative VEGF fluorescence intensity showed the same trend. The BMP-2-positive area was likewise largest in the HP(2:10) group (7.6% at 4 weeks and 11.5% at 8 weeks) compared

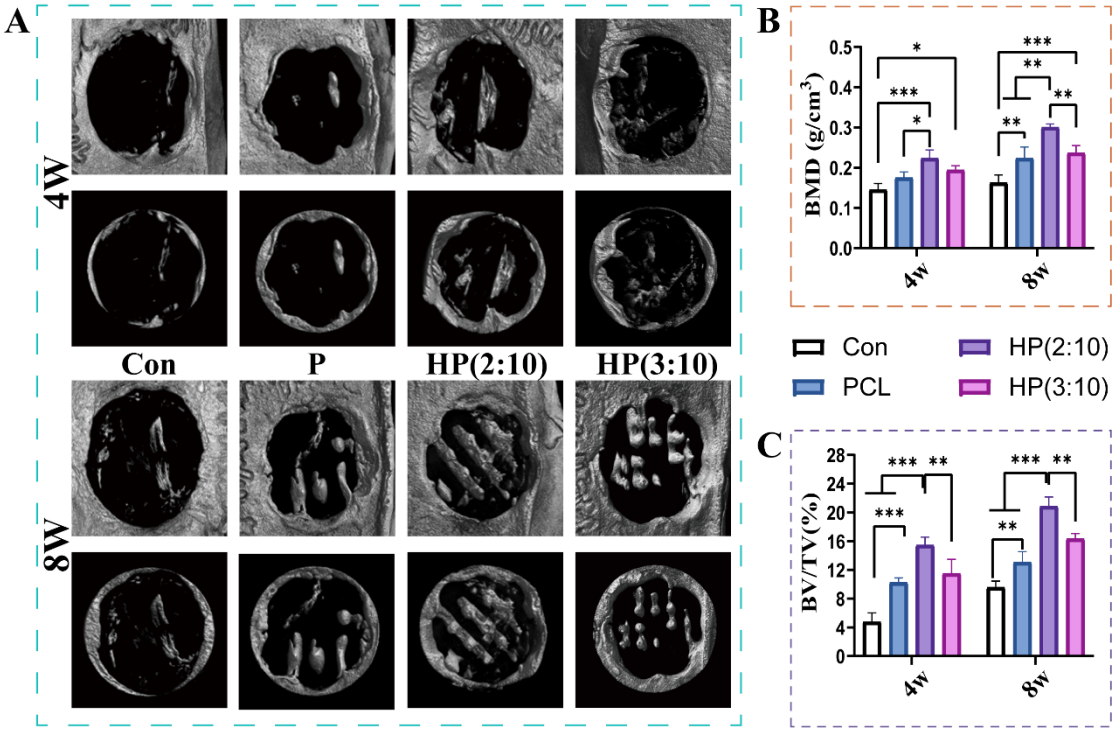



**Figure 7.** Micro-computed tomography assessment of bone regeneration in rat calvarial defects. (A) Representative three-dimensional reconstructions of defects in the Con, P, HP(2:10), and HP(3:10) groups at 4 (4W) and 8 (8W) weeks after implantation. At each time point, the upper row shows the defect and surrounding calvarial bone, and the lower row shows the corresponding top view of the defect region. (B) Bone mineral density (BMD) and (C) bone volume fraction (BV/TV) within the defect region.

Notes: Data are expressed as mean ± SD ($n = 6$ animals per group per time point). Statistical comparisons were performed using two-way ANOVA followed by Sidak's multiple comparisons test. *$p < 0.05$, **$p < 0.01$, and ***$p < 0.001$. Con: Empty defects without implants; P: Pure polycaprolactone (PCL) scaffold; HP(2:10) and HP(3:10): Nano-hydroxyapatite (nHA)/PCL composite scaffolds with nHA:PCL mass ratios of 2:10 and 3:10, respectively.

with the Con group (1.0% and 1.1%), the P group (3.5% and 5.6%), and the HP(3:10) group (4.8% and 10.0%) (all $p < 0.001$; Figure 10C and 10D). The relative BMP-2 fluorescence intensity was also highest in the HP(2:10) group at both time points.

To characterize the local macrophage phenotype, iNOS (M1-associated) and CD163 (M2-associated) were examined through immunofluorescence at 4 and 8 weeks after implantation (Figure 11). In the Con group, a strong iNOS signal was observed with little CD163 signal, particularly at 4 weeks, whereas the scaffold groups showed weaker iNOS and stronger CD163 signals, with the clearest difference in the HP(2:10) group (Figure 11A and 11B). Quantitatively, the iNOS-positive area was highest in the Con group (24% at 4 weeks and 9.7% at 8 weeks) and lower in the scaffold groups. It was lowest in the HP(2:10) group (6% and 2.6%) compared with the P group (11% and 4.9%) and the HP(3:10) group (8% and 4.2%) (all $p < 0.001$; Figure 11C and 11D). The relative iNOS fluorescence intensity followed the same pattern. In contrast, the CD163-positive area was largest in the HP(2:10) group (7.7% at 4 weeks and 13% at 8 weeks) compared with the Con group (1.1% and 2.3%), the P group (3.1% and 5.2%), and the HP(3:10) group (3.6% and 8.4%) (all $p < 0.001$; Figure 11C and 11D). The relative CD163 fluorescence intensity was also highest in the HP(2:10) group at both time points.

## 4. Discussion

The reconstruction of critical-sized bone defects remains a clinical challenge, and synthetic substitutes are needed that provide not only structural support but also an osteoimmune microenvironment favorable for tissue repair.[1,17,18] Although HA-incorporated polymer composites are widely recognized for their osteoconductive properties,[6] the relationship among bioceramic loading, direct osteogenic commitment, and host macrophage responses remains insufficiently defined.[10,11] In this study, scaffolds were printed with identical parameters, and the effects of graded nHA loading on cellular behavior and bone repair *in vivo* were compared. Among the

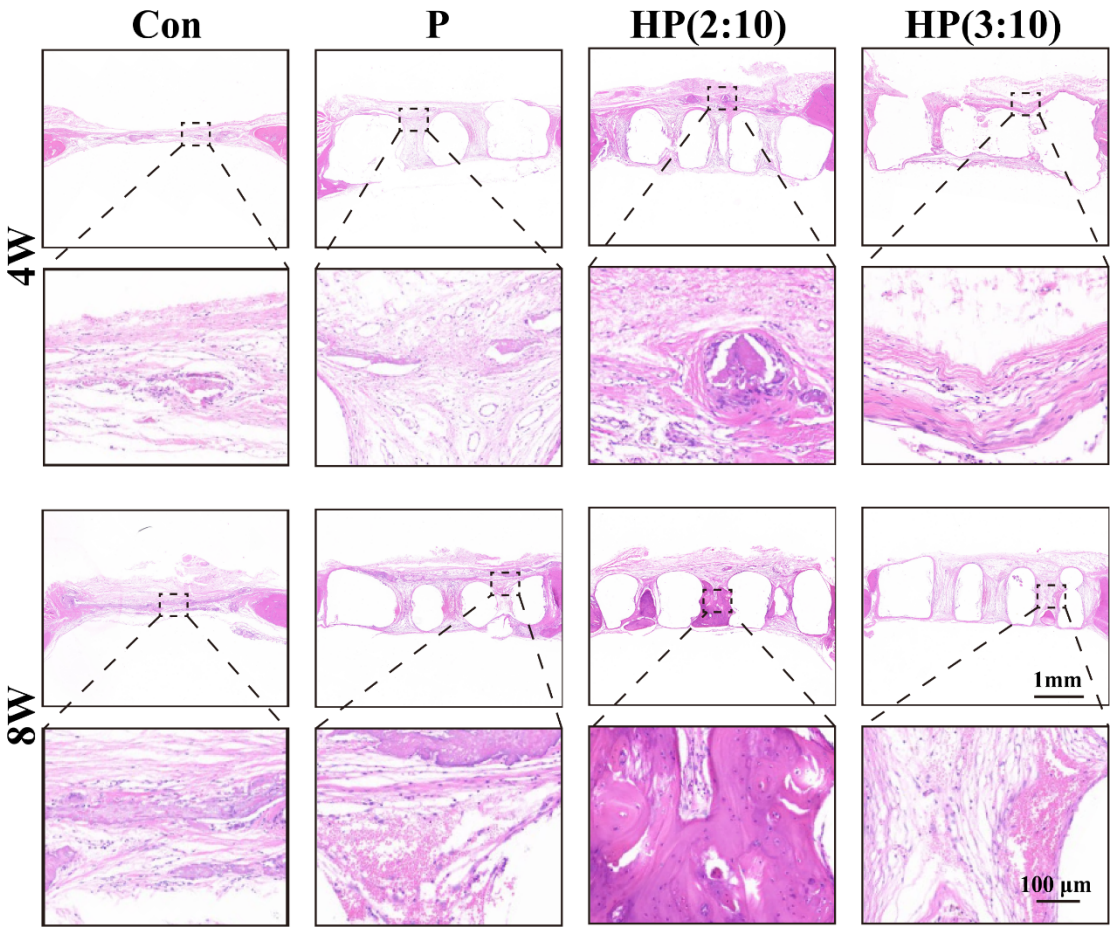



**Figure 8.** Hematoxylin and eosin (H&E) staining of tissue within rat calvarial defects. Representative H&E-stained sections from the Con, P, HP(2:10), and HP(3:10) groups at 4 (4W) and 8 (8W) weeks after implantation. At each time point, the upper row shows low-magnification5×) overviews of the defect region, and the lower row shows higher-magnification 25×) views of the areas outlined by dashed boxes. Scale bars: 1 mm (low-magnification images) and 100 μm (higher-magnification images).

Notes: Con: Empty defects without implants; P: Pure polycaprolactone (PCL) scaffold; HP(2:10) and HP(3:10): Nano-hydroxyapatite (nHA)/PCL composite scaffolds with nHA:PCL mass ratios of 2:10 and 3:10, respectively.

formulations tested, the intermediate HP(2:10) scaffold showed the best overall performance. It supported the highest rBMSC proliferation and ALP activity *in vitro*, was associated with a more M2-like macrophage profile, and was linked to higher BV/TV and BMD, a larger collagen area, and higher VEGF and BMP-2 expression *in vivo*. These responses did not increase monotonically with nHA content, because the higher-loading HP(3:10) scaffold generally provided intermediate or weaker responses than HP(2:10), which may relate to the cellular stress reported at high HA loadings.[12]

The physicochemical properties of a scaffold form the initial interface with cells and host tissue and can influence subsequent biological responses.[37,38] Incorporating nHA into the hydrophobic PCL matrix lowered the apparent water contact angle of the scaffolds, and the angle decreased further with increasing nHA content (HP[2:10], 16.7 wt% nHA; HP[3:10], 23.1 wt% nHA). This is in line with previous reports[39] and may be partly related to the hydrophilic hydroxyl groups on the nHA surface.[34] Because the angles were measured on porous printed scaffolds, they reflect the combined influence of surface chemistry, roughness, and geometry, and the intrinsic wettability of the materials would need to be determined on flat, nonporous films. A lower apparent contact angle has been associated with greater protein adsorption and cell adhesion[40] and with attenuated immune responses.[35] Compressive strength and modulus followed different trends, with the highest strength in the HP(2:10) group and the highest modulus in the HP(3:10) group. This divergence may reflect the

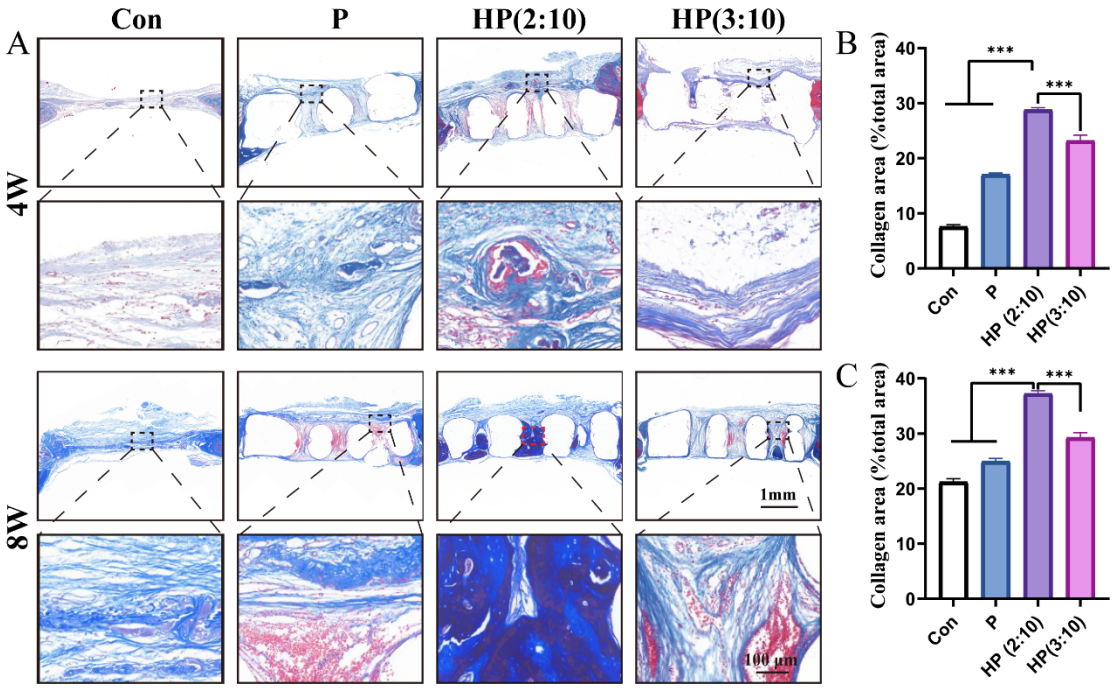



**Figure 9.** Masson's trichrome staining and collagen area quantification in rat calvarial defects. (A) Representative Masson's trichrome-stained sections from the Con, P, HP(2:10), and HP(3:10) groups at 4 (4W) and 8 (8W) weeks after implantation. At each time point, the upper row shows low-magnification (5×) overviews of the defect region, and the lower row shows higher-magnification (25×) views of the areas outlined by dashed boxes. Collagen fibers are stained blue. Scale bars: 1 mm (low-magnification images) and 100 μm (higher-magnification images). (B, C) Collagen area as a percentage of the total analyzed area at (B) 4 weeks and (C) 8 weeks.

Notes: Data are expressed as mean ± SD ($n$ = 6). Statistical comparisons were performed using one-way ANOVA followed by Tukey's post hoc test. ***$p < 0.001$. Con: Empty defects without implants; P: Pure polycaprolactone (PCL) scaffold; HP(2:10) and HP(3:10): Nano-hydroxyapatite (nHA)/PCL composite scaffolds with nHA:PCL mass ratios of 2:10 and 3:10, respectively.

stiffening effect of rigid nHA particles, whereas excessive loading may promote local particle clustering or defects that limit strength. The compressive properties of the printed scaffolds are sufficient to provide mechanical support for cancellous bone regeneration; however, their suitability for load-bearing sites was not evaluated. Strut diameter, macropore size, and porosity (approximately 65%) were comparable among groups, with macropores exceeding 300 μm, and no significant differences were detected. The biological differences observed here are therefore more likely to be associated with composition than with gross scaffold architecture.

Increasing the nHA loading from HP(2:10) to HP(3:10) did not further improve cellular responses. Compared with HP(2:10), the HP(3:10) scaffold supported lower rBMSC proliferation, and cells on HP(3:10) appeared sparser and more rounded, with more dead cells evident in live/dead staining (Figure 3). Moreover, ALP activity on HP(3:10) did not differ from that on the P scaffold, and *Col1* and *Opn* expression at day 14 did not differ from that in the Con and P groups (Figure 4). In related nanocomposite systems, high filler loading has been associated with particle overload and concentration-dependent cellular stress,[12] nanoparticle agglomeration,[13] and oxidative stress,[14] and dose-dependent cytocompatibility has also been reported for other nanoparticle-containing composites.[15] Such processes may contribute to the weaker responses on HP(3:10). Within the two loadings tested, a higher nHA content did not confer additional benefit.

Osteogenic differentiation of mesenchymal stem/progenitor cells is a key step in bone regeneration, and the ability of a scaffold to support it is therefore an important design consideration. In the presence of osteogenic induction medium, the HP(2:10) scaffold increased the ALP activity of rBMSCs, an early marker of osteoblast differentiation, relative to the P and HP(3:10) scaffolds (Figure 4A), and the expression of *Alp*, *Col1*, *Opn*, *Bmp2*, and *Runx2* was highest in the HP(2:10) group for most markers at days 7 and 14 (Figure 4B and 4C). Osteopontin is a phosphorylated, non-collagenous bone matrix glycoprotein implicated in extracellular matrix organization and in the regulation of mineral crystal nucleation,[41,42] so

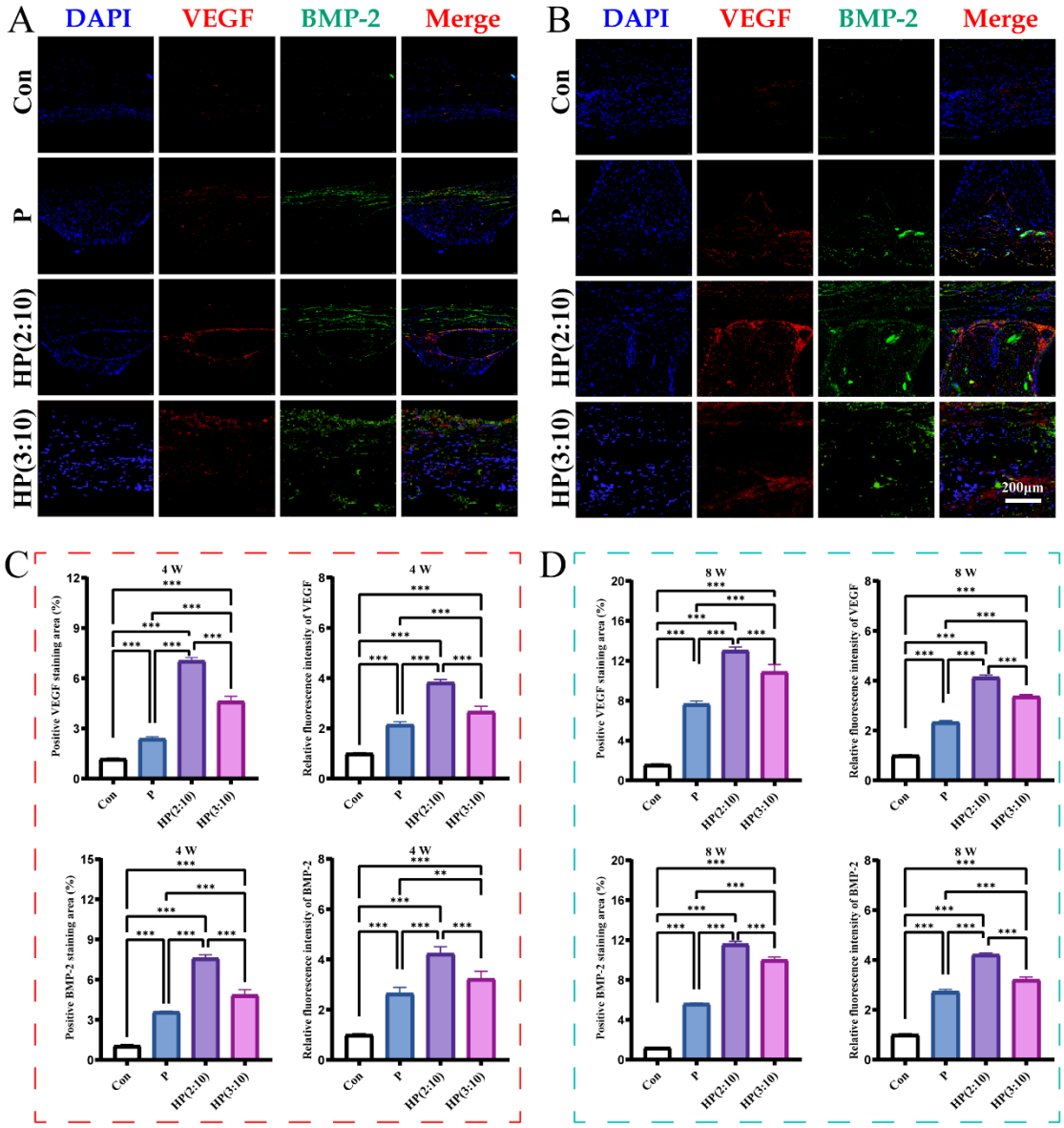



**Figure 10.** Immunofluorescence staining and quantification of vascular endothelial growth factor (VEGF) and bone morphogenetic protein 2 (BMP-2) in rat calvarial defects. (A, B) Representative immunofluorescence images showing VEGF (red), BMP-2 (green), and nuclei (4′,6-diamidino-2-phenylindole [DAPI], blue) at (A) 4 weeks and (B) 8 weeks after implantation. The Con, P, HP(2:10), and HP(3:10) groups are arranged from top to bottom. Merged images show overlays of the three channels. Scale bars: 200 μm; magnification: 40×. (C, D) Quantification of the positively stained area (%) and relative fluorescence intensity for VEGF and BMP-2 at (C) 4 weeks and (D) 8 weeks. For each marker at each time point, fluorescence intensity was normalized to the mean of the group with the lowest mean intensity, which was assigned a value of 1.

Notes: Data are expressed as mean ± SD ($n$ = 6). Statistical comparisons were performed using one-way ANOVA followed by Tukey's post hoc test. $^{**}p < 0.01$ and $^{***}p < 0.001$. Con: Empty defects without implants; P: Pure polycaprolactone (PCL) scaffold; HP(2:10) and HP(3:10): Nano-hydroxyapatite (nHA)/PCL composite scaffolds with nHA:PCL mass ratios of 2:10 and 3:10, respectively.

its higher expression is consistent with a more advanced osteogenic state of rBMSCs on HP(2:10). Because the cells were cultured in induction medium, these results indicate that the scaffold enhanced osteogenic differentiation in the presence of exogenous osteogenic stimuli rather than acting as an autonomous osteoinductive factor. In contrast, HP(3:10) did not outperform the P scaffold for most osteogenic markers.

Macrophage phenotype is increasingly recognized as a determinant of biomaterial implantation outcomes, and

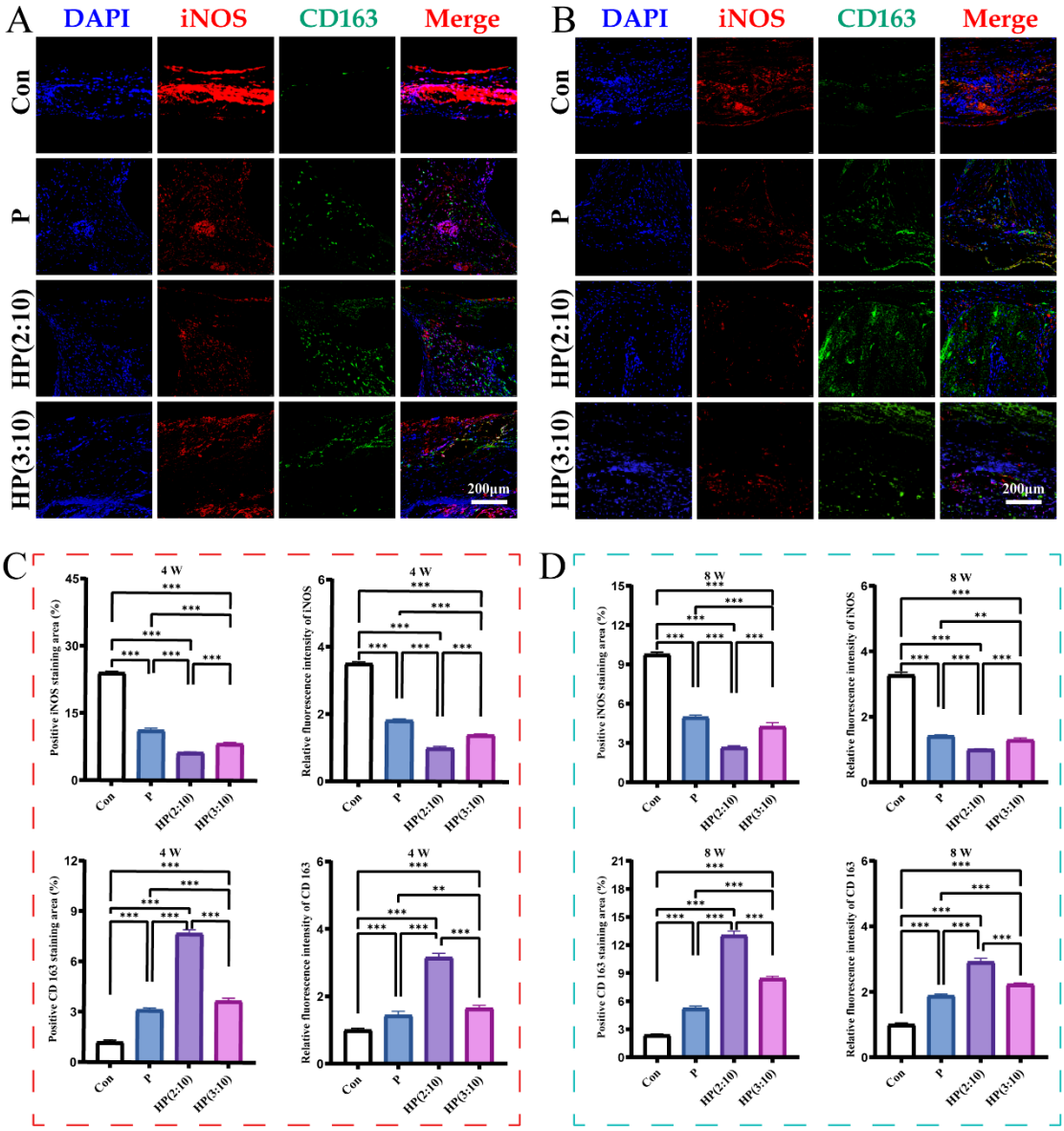



**Figure 11.** Immunofluorescence staining and quantification of inducible nitric oxide synthase (iNOS) and CD163 in rat calvarial defects. (A, B) Representative immunofluorescence images showing iNOS (red), CD163 (green), and nuclei (4′,6-diamidino-2-phenylindole [DAPI], blue) at (A) 4 weeks and (B) 8 weeks after implantation. The Con, P, HP(2:10), and HP(3:10) groups are arranged from top to bottom. Merged images show overlays of the three channels. Scale bars: 200 μm; magnification: 40×. (C, D) Quantification of the positively stained area (%) and relative fluorescence intensity for iNOS and CD163 at (C) 4 weeks and (D) 8 weeks. For each marker at each time point, fluorescence intensity was normalized to the mean value of the group with the lowest mean intensity, which was assigned a value of 1.

Notes: Data are expressed as mean ± SD ($n = 6$). Statistical comparisons were performed using one-way ANOVA followed by Tukey's post hoc test. $^{**}p < 0.01$ and $^{***}p < 0.001$. Con: Empty defects without implants; P: Pure polycaprolactone (PCL) scaffold; HP(2:10) and HP(3:10): Nano-hydroxyapatite (nHA)/PCL composite scaffolds with nHA:PCL mass ratios of 2:10 and 3:10, respectively.

the fate of the repair response, from fibrous encapsulation to tissue integration, is closely linked to macrophage activation.[43] In the present study, RAW264.7 cells cultured on the HP(2:10) scaffold exhibited lower *Il1b* expression and IL-12 secretion and higher *Cd206* expression and IL-10 secretion than cells in the other groups at days 1 and 3 (Figure 5), consistent with an M2-like marker profile. The HP(3:10) scaffold produced intermediate values for the markers examined, without exceeding the effect of HP(2:10). This response may be related to the composition

and surface properties of the composite scaffolds and to the local calcium phosphate ionic environment,[44,45] as calcium and phosphate ions released from bioceramics have been reported to modulate macrophage signaling toward a tissue-repair phenotype.[45] To explore the transcriptomic correlates of this marker profile, RNA-seq was performed as an exploratory analysis comparing macrophages cultured on HP(2:10) with the Con condition. Of the 136 candidate DEGs, 120 were downregulated, and 38 remained significant after Benjamini–Hochberg correction. The candidate DEGs were mainly enriched in the IL-17 and Toll-like receptor signaling pathways at a pathway-level FDR of $Q < 0.05$, whereas the TNF, cAMP, Th1/Th2 differentiation, and NF-κB pathways showed only nominal enrichment (Figure 6). Several genes related to inflammatory signaling and matrix remodeling, including *Fos*, *Ptgs2*, and *Mmp9*, were shared among these pathways. Because IL-17 signaling has been implicated in sustained inflammation and pathological osteoclast activation,[46] these findings are compatible with altered inflammatory signaling in macrophages cultured on HP(2:10).[47,48] The expression changes comprised both downregulated (e.g., *Fos* and *Tlr9*) and upregulated (e.g., *Ccl3*, *Ccl4*, and *Mmp9*) transcripts, reflecting the complexity of the macrophage inflammatory response. As these data were obtained by comparison with the scaffold-free control, inclusion of the P and HP(3:10) groups in future analyses will help define the specific contribution of nHA. The candidate DEG–based patterns are therefore presented as exploratory molecular hypotheses to guide further investigation, rather than as evidence of pathway-mediated immunomodulation.

In the rat calvarial defect model, the HP(2:10) group exhibited higher BV/TV than the Con, P, and HP(3:10) groups at both 4 and 8 weeks. BMD was also higher than that in the Con and P groups at 4 weeks and in all other groups at 8 weeks (Figure 7). Histologically, a dense eosinophilic matrix containing cells within lacunae-like spaces, morphologically consistent with newly formed bone, was observed in the pores of HP(2:10) at 8 weeks, whereas the defects in the Con group were occupied by thin, loose fibrous tissue and the pores of HP(3:10) were mainly filled with fibrous tissue (Figure 8). The collagen area was also largest in the HP(2:10) group (Figure 9). Thus, increasing the nHA content from HP(2:10) to HP(3:10) did not further enhance bone regeneration *in vivo*, in line with the weaker cellular responses observed for HP(3:10) *in vitro*. The VEGF- and BMP-2-positive areas were larger in the HP(2:10) group (Figure 10), indicating higher local expression of angiogenesis- and osteogenesis-related factors.[49,50] Because endothelial markers such as CD31 were not examined, these data reflect pro-angiogenic signaling rather than functional vascularization. The iNOS-positive area was smallest, and the CD163-positive area was largest in the HP(2:10) group at both time points (Figure 11), consistent with a shift toward an M2-dominant marker profile. Because these two markers do not fully characterize the foreign body response, they should not be taken as evidence of complete immune resolution. Taken together, an intermediate nHA loading appeared more favorable for bone regeneration than pure PCL or a higher loading under the conditions tested.

Bone regeneration involves interplay between osteogenic cells and the local immune microenvironment. M2-polarized macrophages have been reported to enhance bone formation and the osteogenesis of mesenchymal stem cells, in part through IL-10 and macrophage-derived extracellular vesicles,[47,48] and favorable macrophage phenotypes have been associated with anabolic and angiogenic cues such as BMP-2 and VEGF.[49] In the present study, the HP(2:10) scaffold was associated with enhanced osteogenic differentiation of rBMSCs under osteogenic induction and a more M2-like macrophage marker profile in RAW264.7 cells, which *in vivo* was accompanied by higher BV/TV, BMD, and VEGF and BMP-2 expression and by a CD163-dominant, iNOS-low macrophage profile at 4 and 8 weeks. These parallel observations are consistent with previous reports that M2-like macrophage polarization is often accompanied by enhanced osteogenesis, and may reflect the close interplay between the skeletal and immune systems described in the field of osteoimmunology.[20,51] Taken together, these findings suggest that an intermediate nHA content in the scaffold is associated with both improved osteogenic activity and a favorable macrophage response, which may jointly favor bone regeneration.

The present study complements recent 3D-printed HA-containing PCL scaffolds designed for immunomodulation and bone repair, including a HA/nanoclay/PCL composite that modulated macrophage responses in a calvarial defect model.[52] Whereas that work evaluated a single ternary formulation, we compared two nHA loadings against pure PCL under identical printing parameters, allowing the effect of nHA content on cell viability, osteogenic markers, and macrophage responses to be examined directly. We further explored the macrophage response using RNA-seq, pointing to the IL-17 and Toll-like receptor signaling pathways as candidate pathways for future testing. The macrophage responses reported here should also be interpreted with the understanding that macrophage activation spans a continuum rather than discrete M1 and M2 states.[21] Although exogenous agents have been reported to shift macrophages toward an M1-like phenotype *in vivo*,[53] and M1/M2 polarization states have been linked to bone homeostasis,[54] marker

shifts in RAW264.7 cells do not by themselves define the immune state of an implanted scaffold. We therefore describe the observed profile as M2-like, and consider it a starting point for characterizing the host response to graded nHA loadings.

This study compared 3D-printed PCL scaffolds with graded nHA loadings, identifying HP(2:10) as a favorable formulation among those evaluated. Nevertheless, these findings represent an initial exploration of composition-dependent osteogenic and immunomodulatory responses. Finer compositional gradients and measurements of particle distribution, ion release, and intracellular reactive oxygen species would clarify loading-dependent effects, whereas crystallinity and surface roughness analyses would help to determine the origin of the surface features of pure PCL. As osteogenesis and macrophage responses were assessed independently, co-culture or conditioned-medium experiments using primary macrophages would help determine their functional relationship. Extending transcriptomic comparisons to additional scaffold groups, independently validating representative transcripts (e.g., by RT-qPCR or protein-level assays), and functionally testing the IL-17 and Toll-like receptor pathways would strengthen mechanistic interpretation. Broader macrophage phenotyping, late-stage mineralization assays, earlier post-implantation assessments, and direct evaluation of foreign body responses and neovascularization would further characterize scaffold–host interactions. Finally, long-term evaluation in large-animal, load-bearing models would help assess mechanical durability, bone regeneration, and tissue integration, informing the translational potential of these scaffolds.

## 5. Conclusion

In summary, this study evaluated 3D-printed HA/PCL composite scaffolds with graded nHA loadings, identifying HP(2:10) as the best-performing candidate among the evaluated compositions. Relative to pure PCL and HP(3:10), HP(2:10) showed improved cytocompatibility and higher ALP activity and osteogenic gene expression in rBMSCs under inductive conditions, and was associated with an M2-like macrophage marker profile *in vitro*. Transcriptomic analysis suggested altered inflammatory signaling, primarily involving the IL-17 and Toll-like receptor pathways. In a rat calvarial defect model, HP(2:10) was associated with higher BV/TV, BMD, and collagen deposition, together with increased VEGF and BMP-2 expression, more CD163-positive and fewer iNOS-positive areas. Collectively, these findings suggest that, among the formulations tested, HP(2:10) supports osteogenic differentiation under induction conditions and is associated with a favorable macrophage marker profile, providing insights into the compositional design of 3D-printed bioceramic–polymer scaffolds for bone regeneration.

## Acknowledgments

None.

## Funding

This research was supported by the National Natural Science Foundation of China (32571583, 82160577, 32000964), the Key Program for Science and Technology Project of Guizhou Province (ZK [2021] 007), the Program for Science and Technology Project of Guizhou Province, Qiankehe Platform Talents ([2021] 5613), the Zunyi City Innovation Team Fund (Zunyi Science Talent [2024] No. 4), and the Guangdong Province Science and Technology Plan Project (2024A1515012265).

## Conflict of interest

We declare that we have no financial and personal relationships with other people or organizations that can inappropriately influence our work; there is no professional or other personal interest of any nature or kind in any product, service, and/or company that could be construed as influencing the position presented in, or the review of, the manuscript entitled.

## Author contributions

*Conceptualization*: Jiaxiang Song, Weihua Huang, Guangquan Zhao, Shuai Huang, Weikang Xu, Qingde Wa

*Data curation*: Qinghong Fan, Qian Du, Yuanhao Lv

*Formal analysis*: Jiaxiang Song, Weihua Huang, Guangquan Zhao, Qinghong Fan

*Funding acquisition*: Weikang Xu, Qingde Wa

*Investigation*: Qinghong Fan, Qian Du, Yuanhao Lv

*Methodology*: Jiaxiang Song, Weihua Huang, Guangquan Zhao, Qingde Wa

*Project administration*: Shuai Huang, Weikang Xu, Qingde Wa

*Resources*: Jiaxiang Song, Weihua Huang, Guangquan Zhao

*Supervision*: Shuai Huang, Weikang Xu, Qingde Wa

*Validation*: Jiaxiang Song, Weihua Huang, Guangquan Zhao, Qinghong Fan

*Visualization*: Jiaxiang Song, Weihua Huang, Guangquan Zhao, Qian Du

*Writing – original draft*: Jiaxiang Song, Weihua Huang, Guangquan Zhao, Qinghong Fan, Qian Du, Yuanhao Lv

*Writing – review & editing*: Shuai Huang, Weikang Xu, Qingde Wa

## Ethics approval and consent to participate

All animal experiments were approved by the Laboratory Animal Welfare and Ethics Committee of the Institute of Biology and Medical Engineering, Guangdong Academy of Sciences (Approval No. 2024021) and were conducted and reported in accordance with the ARRIVE guidelines 2.0. Animals were euthanized by an intraperitoneal overdose of pentobarbital sodium (150 mg/kg), a method considered acceptable for rodents in the AVMA Guidelines for the Euthanasia of Animals: 2020 Edition. The rat bone marrow mesenchymal stem cells (rBMSCs) and RAW264.7 macrophages used in this study were purchased from Feng Hui Biotechnology Co., Ltd. (Hunan, China), and no additional ethical approval was required for their use. No human participants or human samples were involved in this study.

## Consent for publication

Not applicable.

## Availability of data

The RNA sequencing dataset generated in this study is publicly available in the Gene Expression Omnibus (GEO) repository under accession number GSE302053. Additional data supporting the findings of this study are provided within the article and its Supplementary Information.

## AI tools statement

During the preparation of this work, the authors used generative AI tools (ChatGPT, model GPT-6.1 Sol) solely to improve the readability and language of the manuscript. After using these tools, the authors reviewed and edited the content as needed and take full responsibility for the content of the published article.

## References

1. Łuczak JW, Palusińska M, Matak D, *et al*. The future of bone repair: emerging technologies and biomaterials in bone regeneration. *Int J Mol Sci*. 2024;25(23):12766.

   doi: 10.3390/ijms252312766

2. Zhang J, Li S, He H, *et al*. Clinical guidelines for indications, techniques, and complications of autogenous bone grafting. *Chin Med J*. 2024;137(1):5-7.

   doi: 10.1097/cm9.0000000000002691

3. Santoro A, Voto A, Fortino L, *et al*. Bone defect treatment in regenerative medicine: exploring natural and synthetic bone substitutes. *Int J Mol Sci*. 2025;26(7):3085.

   doi: 10.3390/ijms26073085

4. Liang HY, Lee WK, Hsu JT, *et al*. Polycaprolactone in bone tissue engineering: a comprehensive review of innovations in scaffold fabrication and surface modifications. *J Funct Biomater*. 2024;15(9):243.

   doi: 10.3390/jfb15090243

5. Mohan T, Gürer F, Bračič D, *et al*. Functionalization of polycaprolactone 3D scaffolds with hyaluronic acid glycine-peptide conjugates and endothelial cell adhesion. *Biomacromolecules*. 2025;26(3):1771-1787.

   doi: 10.1021/acs.biomac.4c01559

6. Gharibshahian M, Salehi M, Beheshtizadeh N, *et al*. Recent advances on 3D-printed PCL-based composite scaffolds for bone tissue engineering. *Front Bioeng Biotechnol*. 2023;11:1168504.

   doi: 10.3389/fbioe.2023.1168504

7. Jiao Z, Yang H, Zou H, *et al*. Effect of material characteristics of PCL/HA interbody fusion cage on its degradation and mechanical properties. *Int J Bioprint*. 2025;11(2):429-447.

   doi: 10.36922/ijb.7806

8. Aydin MS, Sahin M, Dogan Z, Kiziltas G. Microstructural characterization of PCL-HA bone scaffolds based on nonsolvent-induced phase separation. *ACS Omega*. 2023;8(50):47595-47605.

   doi: 10.1021/acsomega.3c05616

9. Wang FZ, Liu S, Gao M, *et al*. 3D-printed polycaprolactone/hydroxyapatite bionic scaffold for bone regeneration. *Polymers*. 2025;17(7):858.

   doi: 10.3390/polym17070858

10. Abedi N, Sadeghian A, Kouhi M, Haugen HJ, Savabi O, Nejatidanesh F. Immunomodulation in bone tissue engineering: recent advancements in scaffold design and biological modifications for enhanced regeneration. *ACS Biomater Sci Eng*. 2025;11(3):1269-1290.

    doi: 10.1021/acsbiomaterials.4c01613

11. Huang Q, Li X, Fan Q, *et al*. Immunomodulation and bone repair of 3D-printed SrBG/PCL scaffolds with PDA coating. *Int J Bioprint*. 2025;11(4):350-377.

    doi: 10.36922/ijb025210211

12. Andrée L, Joziasse LS, Adjobo-Hermans MJW, Yang F, Wang R, Leeuwenburgh SCG. Effect of hydroxyapatite nanoparticle crystallinity and colloidal stability on cytotoxicity. *ACS Biomater Sci Eng*. 2024;10(11):6964-6973.

    doi: 10.1021/acsbiomaterials.4c01283

13. Müller KH, Motskin M, Philpott AJ, *et al*. The effect of particle agglomeration on the formation of a surface-connected compartment induced by hydroxyapatite nanoparticles in human monocyte-derived macrophages. *Biomaterials*. 2014;35(3):1074-1088.

doi: 10.1016/j.biomaterials.2013.10.041

14. Jin Y, Liu X, Liu H, *et al*. Oxidative stress-induced apoptosis of osteoblastic MC3T3-E1 cells by hydroxyapatite nanoparticles through lysosomal and mitochondrial pathways. *RSC Adv*. 2017;7(21):13010-13018.

doi: 10.1039/c7ra01008g

15. Xu D, Li E, Karmakar B, *et al*. Green preparation of copper nanoparticle-loaded chitosan/alginate bio-composite: investigation of its cytotoxicity, antioxidant and anti-human breast cancer properties. *Arab J Chem*. 2022;15(3):103638.

doi: 10.1016/j.arabjc.2021.103638

16. Sun Z, Liu Q, Wang Z, *et al*. Hierarchical chitosan/polyvinyl alcohol/polyethylene glycol/nonwoven fabric micro/nanofiber composite membrane: a potential biomaterial for wound dressing. *Macromol Res*. 2023;31(12):1209-1215.

doi: 10.1007/s13233-023-00204-y

17. Zhao J, Sun Q, Gu J, *et al*. From "immune silence" to "immune dialogue": modification strategies for bone substitutes based on bone immunomodulatory characteristics. *Front Cell Dev Biol*. 2025;13:1685907.

doi: 10.3389/fcell.2025.1685907

18. Munaò S, Armeli A, Bonfiglio D, Iaconis A, Calabrese G. Immune-guided bone healing: the role of osteoimmunity in tissue engineering approaches. *Int J Mol Sci*. 2025;26(23):11642.

doi: 10.3390/ijms262311642

19. Gou M, Wang H, Xie H, Song H. Macrophages in guided bone regeneration: potential roles and future directions. *Front Immunol*. 2024;15:1396759.

doi: 10.3389/fimmu.2024.1396759

20. Shi X, Xu C, Chen Z, *et al*. Biomaterial-mediated macrophage polarization remodeling and sequential regulation: a potential strategy in bone infections treatment. *Bone Res*. 2025;13(1):96.

doi: 10.1038/s41413-025-00471-8

21. Murray PJ, Allen JE, Biswas SK, *et al*. Macrophage activation and polarization: nomenclature and experimental guidelines. *Immunity*. 2014;41(1):14-20.

doi: 10.1016/j.immuni.2014.06.008

22. Zhang J, Wu Q, Yin C, *et al*. Sustained calcium ion release from bioceramics promotes CaSR-mediated M2 macrophage polarization for osteoinduction. *J Leukoc Biol*. 2021;110(3):485-496.

doi: 10.1002/jlb.3ma0321-739r

23. Yan M, Xiao B, Yosick A, Liu B, Awad HA. Dose-dependent osteoimmunomodulatory effects of amorphous calcium phosphate nanoparticles promote 3D-printed scaffold-mediated bone regeneration. *Bioact Mater*. 2025;51:197-210.

doi: 10.1016/j.bioactmat.2025.05.010

24. Huang W, Huang S, Linghu X, *et al*. 3D-printed mesoporous bioglass/polycaprolactone scaffolds induce macrophage polarization toward M2 phenotype and immunomodulates osteogenic differentiation of BMSCs. *Int J Bioprint*. 2024;10(5):320-339.

doi: 10.36922/ijb.3551

25. Liu J, Zou Q, Wang C, *et al*. Electrospinning and 3D printed hybrid bi-layer scaffold for guided bone regeneration. *Mater Des*. 2021;210:110047.

doi: 10.1016/j.matdes.2021.110047

26. Huang W, Hao L, Cai X, Xiao C, Yin H, Xu W. The osteoinductive and osseointegration properties of decellularized extracellular matrix bone derived from different sites. *Bone Joint Res*. 2025;14(4):292-305.

doi: 10.1302/2046-3758.144.Bjr-2024-0080.R3

27. Lößlein SM, Merz R, Müller DW, Kopnarski M, Mücklich F. An in-depth evaluation of sample and measurement induced influences on static contact angle measurements. *Sci Rep*. 2022;12(1):19389.

doi: 10.1038/s41598-022-23341-3

28. Xu W, Huang W, Cai X, Dang Z, Hao L, Wang L. Dexamethasone long-term controlled release from injectable dual-network hydrogels with porous microspheres immunomodulation promotes bone regeneration. *ACS Appl Mater Interfaces*. 2024;16(31):40581-40601.

doi: 10.1021/acsami.4c06661

29. Love MI, Huber W, Anders S. Moderated estimation of fold change and dispersion for RNA-seq data with DESeq2. *Genome Biol*. 2014;15(12):550.

doi: 10.1186/s13059-014-0550-8

30. Kanehisa M, Goto S. KEGG: Kyoto encyclopedia of genes and genomes. *Nucleic Acids Res*. 2000;28(1):27-30.

doi: 10.1093/nar/28.1.27

31. Kanehisa M. Toward understanding the origin and evolution of cellular organisms. *Protein Sci*. 2019;28(11):1947-1951.

doi: 10.1002/pro.3715

32. Kanehisa M, Furumichi M, Sato Y, Kawashima M, Ishiguro-Watanabe M. KEGG for taxonomy-based analysis of pathways and genomes. *Nucleic Acids Res*. 2023;51(D1):D587-D592.

doi: 10.1093/nar/gkac963

33. Doyle SE, Henry L, McGennisken E, *et al*. Characterization of polycaprolactone nanohydroxyapatite composites with tunable degradability suitable for indirect printing. *Polymers*. 2021;13(2):295.

doi: 10.3390/polym13020295

34. Tian B, Wang N, Jiang Q, Tian L, Hu L, Zhang Z. The immunogenic reaction and bone defect repair function of

ε-poly-L-lysine (EPL)-coated nanoscale PCL/HA scaffold in rabbit calvarial bone defect. *J Mater Sci Mater Med*. 2021;32(6):63.

doi: 10.1007/s10856-021-06533-7

35. Wei X, Lei L, Luo L, Zhou Y, Zheng Z, Chen W. Advances in osteoimmunomodulation of biomaterials after intrabone implantation: focus on surface hydrophilicity. *J Mater Chem B*. 2024;12(43):11089-11104.

doi: 10.1039/d4tb01907e

36. Eosoly S, Lohfeld S, Brabazon D. Effect of hydroxyapatite on biodegradable scaffolds fabricated by SLS. *Key Eng Mater*. 2008;396-398:659-662.

doi: 10.4028/www.scientific.net/kem.396-398.659

37. Kang Z, Wu B, Zhang L, *et al*. Metabolic regulation by biomaterials in osteoblast. *Front Bioeng Biotechnol*. 2023;11:1184463.

doi: 10.3389/fbioe.2023.1184463

38. Ramzan F, Salim A, Khan I. Osteochondral tissue engineering dilemma: scaffolding trends in regenerative medicine. *Stem Cell Rev Rep*. 2023;19(6):1615-1634.

doi: 10.1007/s12015-023-10545-x

39. Bittner SM, Smith BT, Diaz-Gomez L, *et al*. Fabrication and mechanical characterization of 3D printed vertical uniform and gradient scaffolds for bone and osteochondral tissue engineering. *Acta Biomater*. 2019;90:37-48.

doi: 10.1016/j.actbio.2019.03.041

40. Kowalczyk P, Kopeć K, Wojasiński M, Jaroszewicz J, Ciach T. Composite microgranular scaffolds with surface modifications for improved initial osteoblastic cell proliferation. *Biomater Adv*. 2023;151:213489.

doi: 10.1016/j.bioadv.2023.213489

41. Si J, Wang C, Zhang D, Wang B, Zhou Y. Osteopontin in bone metabolism and bone diseases. *Med Sci Monit*. 2020;26:e919159.

doi: 10.12659/msm.919159

42. Singh A, Gill G, Kaur H, Amhmed M, Jakhu H. Role of osteopontin in bone remodeling and orthodontic tooth movement: a review. *Prog Orthod*. 2018;19(1):18.

doi: 10.1186/s40510-018-0216-2

43. Witherel CE, Abebayehu D, Barker TH, Spiller KL. Macrophage and fibroblast interactions in biomaterial-mediated fibrosis. *Adv Healthc Mater*. 2019;8(4):e1801451.

doi: 10.1002/adhm.201801451

44. Liu X, Ouyang L, Chen L, *et al*. Hydroxyapatite composited PEEK with 3D porous surface enhances osteoblast differentiation through mediating NO by macrophage. *Regen Biomater*. 2022;9:rbab076.

doi: 10.1093/rb/rbab076

45. Sun X, Li Z, Wang X, He J, Wu Y. Inorganic phosphate as "bioenergetic messenger" triggers M2-type macrophage polarization. *Adv Sci*. 2024;11(13):e2306062.

doi: 10.1002/advs.202306062

46. Peng R, Dong Y, Zheng M, *et al*. IL-17 promotes osteoclast-induced bone loss by regulating glutamine-dependent energy metabolism. *Cell Death Dis*. 2024;15(2):111.

doi: 10.1038/s41419-024-06475-2

47. Mahon OR, Browe DC, Gonzalez-Fernandez T, *et al*. Nano-particle mediated M2 macrophage polarization enhances bone formation and MSC osteogenesis in an IL-10 dependent manner. *Biomaterials*. 2020;239:119833.

doi: 10.1016/j.biomaterials.2020.119833

48. Kang M, Huang CC, Lu Y, *et al*. Bone regeneration is mediated by macrophage extracellular vesicles. *Bone*. 2020;141:115627.

doi: 10.1016/j.bone.2020.115627

49. Xie Y, Hu C, Feng Y, *et al*. Osteoimmunomodulatory effects of biomaterial modification strategies on macrophage polarization and bone regeneration. *Regen Biomater*. 2020;7(3):233-245.

doi: 10.1093/rb/rbaa006

50. Grosso A, Burger MG, Lunger A, Schaefer DJ, Banfi A, Di Maggio N. It takes two to tango: coupling of angiogenesis and osteogenesis for bone regeneration. *Front Bioeng Biotechnol*. 2017;5:68.

doi: 10.3389/fbioe.2017.00068

51. Gao X, Dong S, Zheng X, Si Y, Zhang C. Sequential polarization of macrophages: an immunomodulatory strategy for novel bone repair materials. *Regen Biomater*. 2026;13:rbag144.

doi: 10.1093/rb/rbag144

52. Li X, Wen Z, Song J, *et al*. Three-dimensional-printed hydroxyapatite/nanoclay/polycaprolactone composite scaffold for immunomodulation and bone defect repair. *Int J Bioprint*. 2025;11(3):434-456.

doi: 10.36922/ijb025170162

53. Qin G, Li P, Zhang M, *et al*. Exopolysaccharide from Rhizopus nigricans modulates antitumor immune responses by promoting tumor-associated macrophage polarization toward the M1 phenotype in C57BL/6J mice. *Russ J Bioorg Chem*. 2024;50(6):2519-2528.

doi: 10.1134/s1068162024060049

54. Li L, Zhang Y, Huang S, *et al*. Metabolic reprogramming in macrophages: the central role of lipid metabolism in bone homeostasis. *Bone Res*. 2026;14:108.

doi: 10.1038/s41413-026-00590-w